8-29-2012 12:00 AM

Investigations of Zeolite Growth by Atomic Force Microscopy (AFM)

Donghan Chen
The University of Western Ontario

Supervisor
Yining Huang
The University of Western Ontario

Graduate Program in Chemistry
A thesis submitted in partial fulfillment of the requirements for the degree in Master of Science

Recommended Citation

Chen, Donghan, "Investigations of Zeolite Growth by Atomic Force Microscopy (AFM)" (2012). *Electronic Thesis and Dissertation Repository*. 835.
https://ir.lib.uwo.ca/etd/835

INVESTIGATIONS OF ZEOLITE GROWTH BY ATOMIC FORCE MICROSCOPY (AFM)

(Spine title: Atomic Force Microscopy studies of Zeolites)

(Thesis format: Integrated Article)

by

Donghan Chen

Graduate Program in Chemistry

A thesis submitted in partial fulfillment
of the requirements for the degree of
Master of Science

The School of Graduate and Postdoctoral Studies
The University of Western Ontario
London, Ontario, Canada

THE UNIVERSITY OF WESTERN ONTARIO
School of Graduate and Postdoctoral Studies

CERTIFICATE OF EXAMINATION

Supervisor	Examiners
Dr. Yining Huang	Dr. T.K. Sham
Supervisory Committee	Dr. Zhifeng Ding
	Dr. Andy (Xueliang) Sun

The thesis by

Donghan Chen

entitled:

Investigation of Zeolite Growth by Atomic Force Microscopy (AFM)

is accepted in partial fulfillment of the
requirements for the degree of
Master of Science

Date

Chair of the Thesis Examination Board

Abstract

Zeolites are microporous materials that have been used extensively in various fields. A better understanding on their crystallization process is important for their investigations. Atomic force microscopy (AFM) is a powerful tool for studying the growing traces on the crystal surface, providing information regarding the relation between surface events and framework structure. This thesis mainly focuses on the surface investigation of several zeolites and microporous materials. ZSM-11 single crystals were synthesized under hydrothermal conditions, and their crystallization process was monitored by AFM, PXRD, SEM, and SSNMR. SAPO-34 prepared under both HTS and DGC conditions showed morphological differences that are related to their growing conditions. Finally, SAPO-37 crystals were examined and showed different terminal structures. Studies on ZSM-39 revealed different growth rates on the two types of faces of the crystal.

Keywords

Zeolites, zeolite frameworks, single crystal, crystal surface structure, crystallization, ZSM-11, ZSM-39, SAPO-34, SAPO-37, atomic force microscopy

Co-Authorship Statement (where applicable)

The following thesis contains materials from previously published manuscripts written, or edited by Donghan Chen and his colleagues mentioned below. Dr. Yining Huang, as the supervisor of Donghan Chen, is co-authored on all materials presented in this thesis. Some of SAPO-34, all SAPO-37 crystals were provided by my Ms. Lu Zhang and Ms. Jenifer Bates in Dr Yining Huang's group. ZSM-39 crystals were provided by Ms. Zheng Sonia Lin who is also in this group.

Acknowledgments

I would like to express my deepest appreciation to my supervisor, Dr. Yining Huang, for his constant support, insightful suggestion, and sincere encouragement. This thesis would not be possible without his help in so many ways. His guidance during my Master's study will definitely benefit my further career.

I sincerely thank Dr. Heng-Yong Nie, as I learned so much about AFM under his guidance for surface analysis. The time we spend together for discussing research problems will be a great memory.

I am also grateful to Dr. Nicolas Payne, who gave great lectures on crystallography course and provided much help on my research regarding the crystal structure.

My gratitude also goes to all my thesis examiners Dr. T. K. Sham, Dr. Zhifeng Ding, and Dr. Andy Sun for reading my thesis and providing valuable suggestions.

I would like to thank Dr. Lyudmila Goncharova for her exciting lectures of Surface Science course, Dr. Matthew Willans for his help in NMR operation, and Ms. Grace Yau from Earth Science for her help on XRD experiments. I also wish to thank Tim Goldhawk and Todd Simpson from Western Nanofabrication Facility for helping me on SEM.

Great appreciation goes to my colleagues in Dr. Yining Huang's group. They are Dr. Andre Sutrisno, Margaret Hanson, Lu Zhang, Jun Xu, Tetyana Levchenko, Adam MacIntosh, Yue Hu, Zheng Sonia Lin, and Peng He.

Last but not least, I would like to thank my dear parents and brother. And it would be impossible to say enough about my fiancée, Lifang. Their love and support are the reasons for what I can be today.

Table of Contents

List of Figures

List of Appendices

List of Abbreviation

$ALPO_4$	Aluminophosphates
CHA	Chabazite
CP	Cross polarization
D6R	Double 6-ring
DES	Deep Eutectic Solvents
DGC	Dry gel conversion
DPHMII	*N, N*-dipropylhexamethyleneiminium iodide
FAU	Faujasite
IZA	International Zeolite Association
LTA	Linde Type A
MAS	Magic-angle spinning
MEL	Mobil Eleven
MFI	Mobil Five
MOF	Metal-organic framework
MTN	Mobil Thirty-Nine
n-MR	*n*-membered ring
NMR	Nuclear magnetic resonance
ppm	parts per million (chemical shift)
SAPOs	silicoaluminophosphates
SDA	Structure-directing agent
SEM	Scanning electron microscopy
Si/Al	Silicon to aluminum ratio
SOD	Sodalite

SSNMR	Solid-state Nuclear magnetic resonance
TTMSS	Tetrakistrimethylsilylsilane
XRD	X-ray diffraction

To my dear parents, my brother, and Lifang

Chapter 1 Introduction

1.1 Zeolites and Zeolite Frameworks

Zeolites are crystalline silicates or aluminosilicates with open channel or cavities. They are the most well known family of microporous materials, which is usually referred to as molecular sieves. Zeolites are widely used in industry as sorbents, ion exchangers and catalysts. Each zeolite has a unique framework topology that is composed of Si or Al tetrahedral sites connected via Si-O-Si or Si-O-Al linkages. Zeolites were first discovered from natural minerals in 1756 by Swedish mineralogist Axel Fredrik Cronstedt [1], who found the material produces a large amount of steam upon boiling in water. The name of “zeolite” is derived from Greek that means “boiling stone”.

For those zeolites that are pure silicate, their frameworks are electrically neutral; and for those frameworks with Si^{4+} sites partially substituted by Al^{3+} sites, each AlO_4 generates a negative charge in the framework. Therefore, extra cations usually coordinate with the negatively charged oxygen atoms surrounding the aluminum. The labile coordination of the cations to framework makes the ion-exchange happen easily.

The typical formula of a zeolite can be described as:

$$\mathrm{M}_{\frac{x}{n}}^{n+}(\mathrm{AlO_2})_x(\mathrm{SiO_2})_y \cdot m\mathrm{H_2O}$$

where M represents the extra-cation for charge balancing. Depending on the reaction composition, M^{n+} may be inorganic cation or organic group. The ratio of silicon to aluminum in zeolite ranges from 1 to infinity. The lower limit of 1 owns to that the framework structures cannot form Al-O-Al linkages.

1.1.1 Development in zeolite materials

Although zeolite was found in 1756, first hydrothermal synthesis of zeolite was not reported until 1862 by St. Claire [2]. His early attempt mainly focused on simulating the mineral forming conditions under high temperature and high pressure (T>200˚C, P>10000kPa). During 1930's, R. Barrer and J. Sameshima started systematic studies on zeolite synthesis, and ultimately found conditions for synthetic zeolite at autogenously produced pressure and temperature from 25°C to 200°C [3]. As continuous discovery of natural zeolites and invention of synthetic zeolites A, X and Y in 1950's [4,5], zeolites started performing as adsorbents in industrial separations and purifications. This application in industrial led the development of zeolitic synthesis and provided possibility of later boom of engineering for commercial zeolites.

Molecular sieve are material with micro scale pores that can be used as adsorbents for gases and liquids. Beside zeolites, another important type of molecular sieve is aluminophosphate ($AlPO_4$)-based materials. They were discovered by the workers at Union Carbide in 1982 [6]. The $AlPO_4$s have very similar framework strucutres to those of the zeolites. Instead of compositing by Si-O-Si or Si-O-Al bridges in the zeolites, $AlPO_4$ are formed by Al-O-P linkages [7]. Since the frameworks of $AlPO_4$s are neutral, consequently, the substitution of P and Al atoms by Si is an ideal method to generate negatively charged framework. Therefore, it increases greatly the possibility of using the resulting materials, silicoaluminophosphates (SAPOs), as acid catalysts [7]. The possible linkages in SAPOs are Si-O-Al, Si-O-Si and P-O-Al, while Si-O-P linkages are not stable in framework structure [7].

1.1.2 Zeolite framework structure

The framework structure of zeolite is of great importance since it determines many of the material properties. The topology of a zeolite can be described as zeolite framework types regarding the connectivity preference of their identifiable structural units. Each framework type simply describes the topological arrangement of the building units without concerning its chemical composition. Therefore, it is possible for several different materials sharing the same framework type. For example, zeolite framework type faujasite – with a framework type code of FAU - is a common type that many materials can be classified into this type such as zeolite X, zeolite Y, zeolite faujasite and SAPO-37. To date, there are more than 200 types of framework types assigned to three letter codes according to the International Zeolite Association (IZA) data base [8].

Figure 1.1 Illustrative schemes of TO_4 tetrahedral structure in different models [9].

The primary building units in zeolites are TO_4 tetrahedral sites (T=Si or Al), where the T atoms locate at the center of the tetrahedra (Figure 1.1). The O-T-O bond angles in the TO_4 sites have ideal value of 109°28' which guarantees each T atom's linking to four oxygen atoms stably. Oxygen atoms can bridge T sites, which makes it possible for linking TO_4 sites together [9]. As the angle of T-O-T could vary from 125° to 180°, a number types of simple geometric shaped structures, referred to as second building unit (SBU), thus could be formed. Among different SBUs, *n*-membered rings are most common ones, which are composed with certain number of T sites with same number of O atoms bridging each two neighboring tetrahedral sites. For example, a 6-membered ring (6MR) is built up by six T-sites and the same number of oxygen atoms bonding in between (Figure 1.2). More complicated SBUs can be built by linking the *n*-rings. For example, two 6MR can link together and form a double 6-ring (D6R). The ring structures are considered to be the origin of the pore and channel in zeolites. Based on their pore sizes, 8MR, 10MR and 12MR are considered as small, medium, large porous structure with diameter around 4.1 Å, 5.6 Å and 7.4 Å respectively. For 6MR or smaller rings, the pore sized is around 2 Å so that ions in the pores are strictly confined. For rings that contain 14 T atoms (14MR) and more, the pore sizes are larger than 8 Å therefore they are considered as extra-large pore openings. Different open structures determine the properties of zeolites.

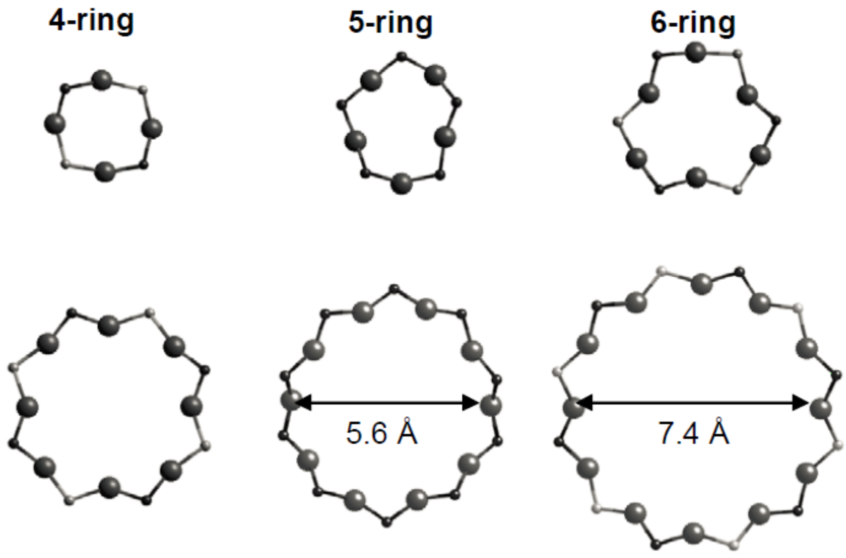

Figure 1.2 Illustrative schemes of *n*-membered rings [10].

Following the SBUs, the next level of building structures are cages, chains, and channels made up by n-membered rings. Cages are polyhedral units built by several n-membered rings whose pore opening sizes are usually very small. Figure 1.3b shows a sodalite cage (structural unit of zeolite Sodalite) built by 4MRs and 6MRs. The zeolite A's structure is made up by linking sodalite cages with double 4-rings (Figure 3c). Chains and channels are one-dimensional building structures that could also be found in some zeolite frameworks. They are usually formed by a series of rings linking one to another in certain direction. Zeolite framework then could be building by stacking the chain structures.

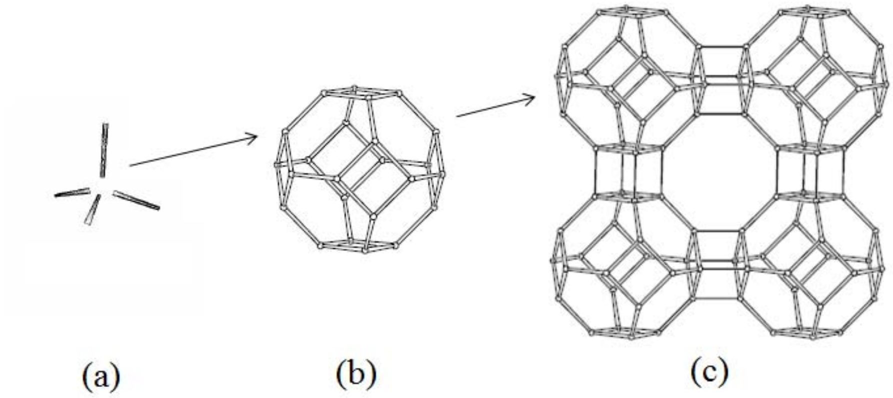

Figure 1.3 Schemes of building structures (a) TO_4 site; (b) Sod cage; (C) framework structure of Zeolite A.

1.1.3 Importance of zeolites in industrial applications

Due to their large intracrystalline surface, shape selective properties and catalytic performance as solid acids, zeolites are commercially important as good ion exchangers, adsorbents and catalysts in a variety of industrial processes [9,10]. One of the most worth-mention examples in ion exchanging is the use of zeolite A as detergent builder. With framework composition of Si/Al=1, zeolite A has the maximum capacity of ion exchanging and thus was regarded as an ideal water softener. During the process of water softening, the excess Ca^{2+} and Mg^{2+} ions in "hard" water get into the zeolite A structure that contains Na^+ ions. As Ca^{2+} and Mg^{2+} ions have stronger binding with the framework sites, they will replace the Na^+ ions and thus be confined in zeolite cages. Another important application of zeolite is the use of absorbents. Depending on the different pore sizes, zeolites perform as separating host for gas, solution and bulk materials. When different molecules diffuse through zeolites, some of them may not be able to pass the zeolite due to the shape selectivity of framework structure. In addition, the large intracrystalline surface of zeolites offers significant adsorbent area. Zeolite is one of the most important solid catalysts in industrial chemistry. Regarding its ability as solid catalyst, many fields especially chemistry in petroleum industry are using zeolites as catalysts.

1.2 Synthesis of Zeolites

Zeolites can be synthesized by a variety of methods [10,11]. Among many methods, hydrothermal synthesis (HTS) is most widely used. In HTS, the reaction happens at a temperature of 100-200°C in a steal autoclave with the presence of zeolite framework elements, structure directing agent (SDA) and water as solvents [11]. In general, alkaline medium is an ideal crystallization condition for zeolite as high pH value helps deprotonation of the silanol groups [9]. Low pH condition easily directs an aggregation of dense phase of alluminosilicate [9]. The initial chemical composition affects the final product crucially, but the product can hardly be designed precisely by the initial composition. The reaction in HTS is actually not ideally homogenous in both liquid phase and solid phase. Other synthesis parameters such as temperature, pressure and heating time could also influence zeolite formation; therefore, zeolite synthesis is a very complex process.

In the synthesis of zeolites, normally a structure directing agent (SDA) is needed to assist forming the zeolite framework [12]. Most SDAs are in the form of organic species, and also some are inorganic cations like Na^+ or K^+.[10] The precise function of SDA has been under debate and discussion for a long time and still opens to questions. One possible theory of the role of SDA is that organic species organize the tetrahedral silica-alumina units with its own morphology so that certain framework could be built [12]. Inorganic templates relatively cost much lower than organic template, but organic templates provide more stable and some of the framework structure can only successfully synthesized with organic species. Fluoride (F^-) species are used in some of the zeolite synthesis. In the presence of F^-, the crystallization rate can be decreased so that some large crystals with high crystallinity can be produced [13]. The fluoride ion thus works as a mineralizing agent in zeolites synthesis.

1.3 Zeolite Growth Mechanisms

Theories of crystal growth are significantly depending on crystal surface structure. One of the mostly used crystal surface model is provided by Kossel (Figure 1.4a) [10,14]. In this model, atoms are considered as cubic growth units and crystal grow by forming atomic layers. With this growth mechanism, each layer of atoms is limited by its step and the layer between two steps is referred as a terrace. According to this model, growth will proceed by the attachment of growth units. The surface may produce growth structures like growth units, clusters, or vacancies. Since kinks provide the most stable growth sites besides a small number of vacancies, growth units prefer to attach at the kink site during growth (Figure 1.4b). Therefore, the kink will move along the step and keep proceeding step advancement until it reaches the face edge. During the step's moving, new growth units attached on the terrace form two-dimensional nuclei and thus produce new kinks. Crystals at solutions that is not high supersaturation enough for surface nucleation can still grow by spiral growth mechanism (Figure 1.4c) [15]. The crystal surfaces are intercepted by dislocations, and this will generate surface steps. The growth units in low supersaturation are only able to attach at the kink sites. Therefore, spiral growth feature is formed.

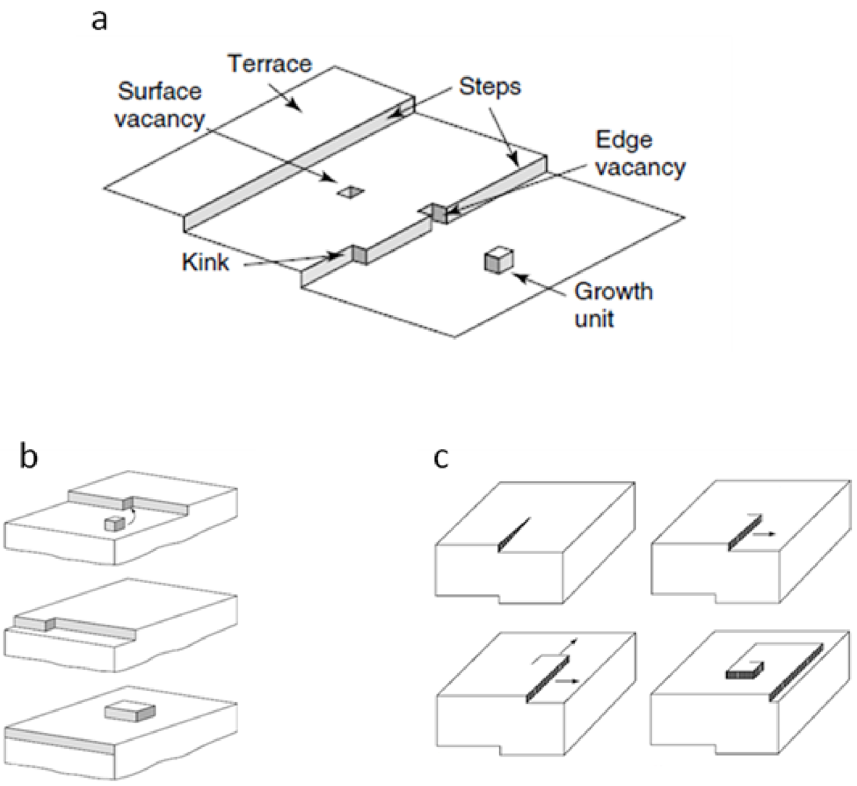

Figure 1.4 (a) Kossel model of a crystal surface; (b) illustration of layered growth; (c) illustration of spiral growth [10].

Generally, crystals of zeolite grow in supersaturated solution or gels with framework-forming elements and SDA. Growing behavior and mechanisms rely on a series of conditions such as reaction temperature, pressure, ratio of framework-forming elements and template. Depending on the surface roughness, three mechanisms of zeolite growth are commonly used for classifying the different growth processes, including adhesive growth, birth and spread and spiral growth (Figure 1.5A) [10]. In high supersaturated solution, zeolites tend to grow rapidly under adhesive mechanism that small nuclei grow by attaching each other and forming rough surfaces particles. Zeolites in final products are more likely to follow the other two mechanisms in lower supersaturated solution. In birth and spread growth, 2-dimensional nuclei much smaller than crystal dimensions are first occur on crystal surface as the “born” process and then spread to enlarge the size. In spiral growth, line defect caused by crystal dislocation leads to a spiral structure on the surface along the line defect.

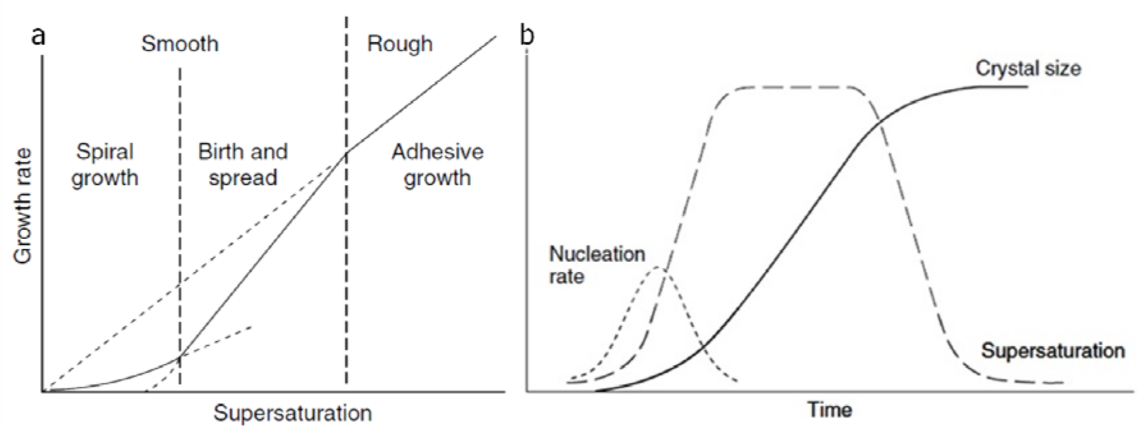

Figure 1.5 (a) Simplified theoretical diagram showing mechanisms of growth as a function of supersaturation; (b) Schematic representation of the zeolite synthesis process showing the evolution of nucleation and growth rates, as well as supersaturation as a function of time [10].

Figure 1.5B shows the plots of the rate of nucleation, crystal size growth and the supersaturation as a function of synthesis time. The number of the crystals grows rapidly with the rate of nucleation increases just after a period of induction time, and may maintain after nucleation rate decreasing to zero. Supersaturation stays at a high level after the increase in the induction period and decreases to zero with the crystal growth. Crystals enlarge their size until the nutrients exhausted.

1.4 Atomic Force Microscopy (AFM)

Atomic Force Microscopy (AFM) is an excellent technique for surface morphology analysis due to its high spatial resolution (nanometer scales in the lateral dimension and sub-nanometer scales in height) in real space and capability of working under different environments. AFM could achieve morphology imaging, surface parameter measurement, and even nanoscale manipulation on material surface. The AFM is a powerful tool for imaging, measuring, and manipulating materials at the nanoscale. By scanning an extremely sharp tip on the sample surface, AFM could detect surface properties and construct the surface morphology. The modern day AFM has been labeled as the most versatile and widely recognized technique among the instruments applied to nanoscience and nanotechnology.

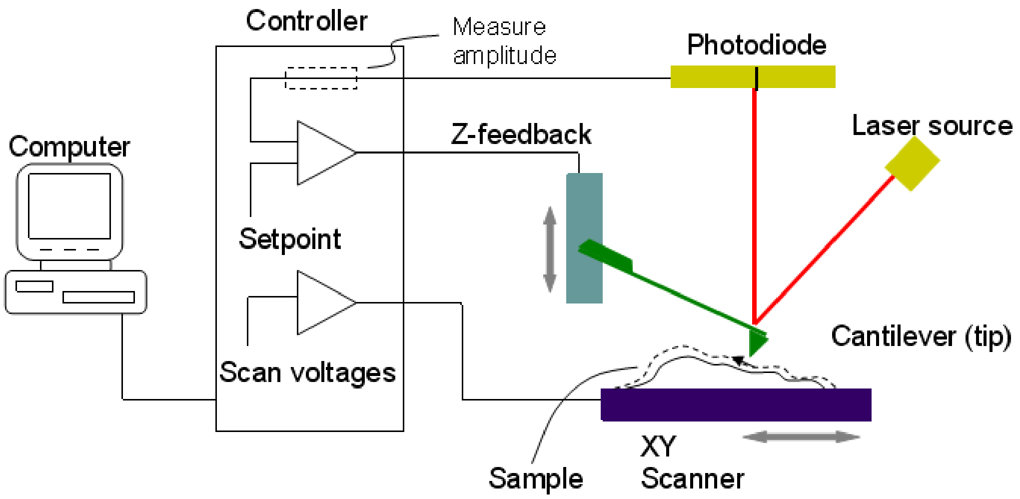

Figure 1.6 Scheme of a typical AFM system.

Distinguished from its precursor, Scanning Tunneling Microscopy (STM), which relies on tunneling current between scanning tip and sample surface atoms, AFM mechanically contacts with materials directly. Therefore, AFM provides possibility of observation on almost any type of materials. On the other hand, scanning tip could also work under liquid, which offers the chance for observing crystals in solution and in situ monitoring crystallization process.

Working principle of AFM is also relatively simple among the advanced characterization techniques. Typically, AFM contains three main parts shown in Figure 1.6: scanning system, controller and computer. Samples are usually located on a piezoelectric scanner which provides precise movement on *x, y* and *z* direction. A very sharp tip attached to a soft cantilever scans on sample surface line by line with the motion of piezoelectric scanner. During the scanning, controller adjusts z canner to maintain a constant tip-sample force value to make sure tip-sample distance as a constant value. At the backside of the tip, a laser beam comes out of laser source and reflects to a photodiode detector. With the monitoring of the laser beam signal, height change and deflection information of tips could be captured precisely by the controller. Thus, three dimensional morphology images could be constructed in three dimensions by recording height change during lateral dimensional scanning.

AFM achieves extremely high resolution on sample surface morphology depending on sharpness of the probe tip, precision of the scanner and the optical detection system. Probe tip usually has radius of a few nanometers (~10nm), which only has a small amount of atoms at the end. High sensitivity piezoelectric ceramic provides accurate three-dimensional displacement. Long path of laser beam amplified slight change of the tip and laser signal could be captured precisely by photodiode. Tip-sample interaction also helps AFM achieve atomic level resolution. Tip-sample interaction may be described by the rule of Lennard-Jones potential [ω(r)] [16] which deals with the ideal interaction between two atoms:

$$\omega(\mathrm{r}) = -\frac{\mathrm{A}}{\mathrm{r}^6} + \frac{\mathrm{B}}{\mathrm{r}^{12}} \tag{1}$$

Where r is the distance between two bodies and A, B are known to be 10^{-77}Jm^6 and 10^{-134}Jm^{12} respectively. Force interaction then is

$$\mathrm{F} = -\frac{\mathrm{d}\omega}{\mathrm{dr}} = -\frac{6\mathrm{A}}{\mathrm{r}^7} + \frac{12\mathrm{B}}{\mathrm{r}^{13}} \tag{2}$$

Force-distance curve is shown in Figure 1.7.

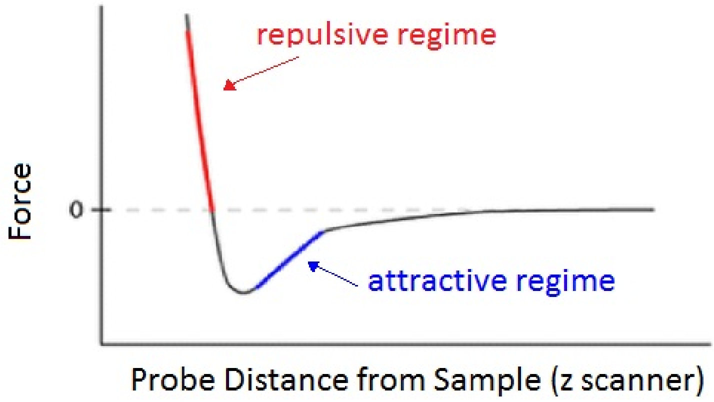

Figure 1.7 Force-distance curve of two atoms.

The curve increases steeply when separation distance is smaller than 0.4nm, which provides the sensitivity to detect slight height change from repulsive force.

Different scanning modes are available, depending on several sample-tip relative motion types. In contact mode, tip scans under an applied force and feedback system keeps tip-sample interaction force in a constant value. In dynamic mode, oscillating cantilever beats on the sample surface to minimize the tip-sample contact effect and improves the ability on soft materials detection. The oscillation amplitude and phase change are taken as parameters to report surface information. Therefore, AFM not only depict morphology information but also could present material surface property by phase shift information.

Although AFM is a powerful tool for characterization a variety of materials in different environments, it still has some limitations. As the sharpness of the tip, AFM used in this thesis can only scan for 45μm^2 in image size and the scanning speed is much slower than other characterization methods like electron microscopy. Unsuitable tip introduces image artifacts in the morphology image. Artifacts are mainly due to tip shape change, such as sticking impurities from sample surface, or a small piece knocked off from the tip end. As a detector originally designed for flat materials, AFM can hardly work on morphology with steep walls or overhangs.

1.5 AFM Studies of Surface Structure of Zeolites (Literature Review)

The advancement in AFM technique brings new possibilities to investigate the surface events that occur during crystal growth [10]. By studying detailed morphology information provided by AFM in nanometer level, one can better understand the growth mechanisms and growth fundamentals from a new point of view.

Initially, AFM studies on microporous materials were focused on the observation of porous structure at the surface termination on natural zeolites [17,18]. Nonetheless, zeolite surface with the presence of steps that indicates the "birth and spread" growth mechanism were reported by Yamamoto et al and Anderson et al in late 1990s [19]. And Anderson's work in zeolite Y is the first AFM study on synthetic zeolite [19]. Inspired by these ideas, there came a number of AFM investigations on a variety of zeolites or other microporous materials, such as zeolite A [20-22], zeolite X/Y [23,24], zeolite L [25]. In all these studies, AFM provide possibilities to investigate growth units. For a long time, the presented surface features are mainly the steps and terraces, which makes some authors conclude the "birth-and-spread" is the preferential growth behavior. However, later on some studies showed spiral growth on zeolite A [26], suggesting that the different growth behavior is possible. In very recent years, not only zeolites, but more microporous materials were investigated by AFM, such as SAPO-base material [27,28], Zincophosphate materials [29], and metal-organic frameworks (MOFs) [30]. These studies are also focused on the surface morphology. In addition, some studies show morphological information of different facets on same crystal [25,31].

One of the advantages of AFM for crystal studies is its ability of working under liquid environments [32]. A lot of in-situ studies have been carried out on zeolite surfaces to investigate crystal growth [29], dissolution [8,33,34], re-crystallization [30] in solution. In-situ AFM is a more direct approach to monitor the change in crystal surface.

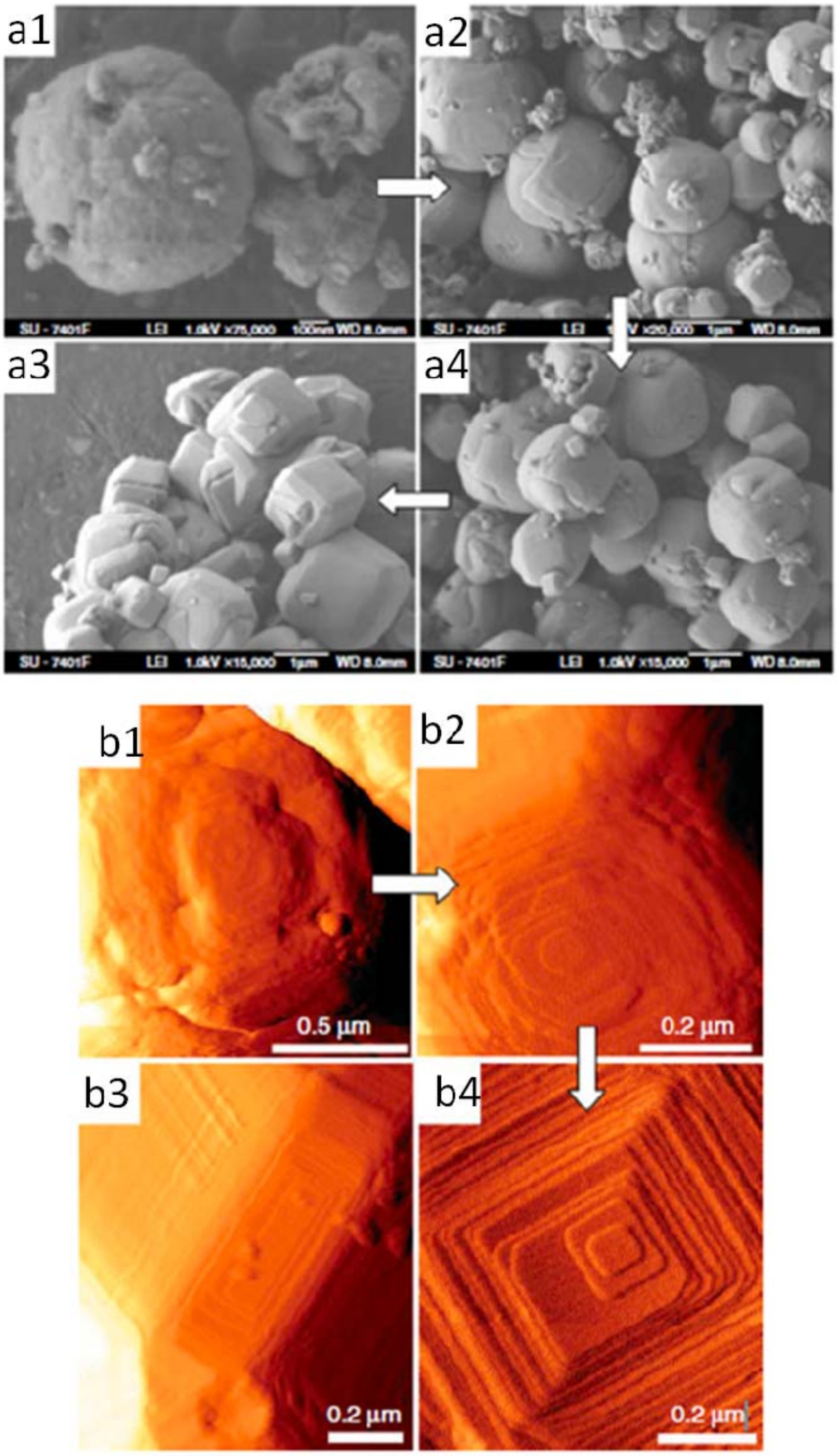

Figure 1.8 SEM and AFM studies on Zeolite A [31].

To better illustrate the advantages of AFM in zeolite studies, an exemplar study [31] of zeolite A is shown in this section. The morphology evolution is monitored by both SEM and AFM. In Figure 1.8a, the images of crystals with reaction time of 2.5 h (a1), 4 h (a2), 8 h (a3), and 20 h (a4) are shown, respectively. Figures 8b shows AFM images of zeolite A samples with following reaction time: 4 h (b1), 8 h (b2), 20 h (b3-b4). The 2.5 h sample in SEM image presents ball-shaped crystals, which show obvious adhesive growth mechanism as particles grow by attaching to each other. With the extension of the reaction time, 4 h sample in SEM show round shaped crystals with rich surface features. The AFM image of 4 h shows that the round shaped crystal has not had a face that is fully developed. The SEM image of 8 h sample (a3) shows the crystal have cubic morphology with round corners and edges, and its corresponding AFM image (b2) presents well defined terrace structure. The 20 h sample in SEM image (a4) presents typical cubic facets and its AFM images on both (100) and (110) are shown in b3 and b4, respectively. The AFM detection in this study provides more detailed surface features comparing with SEM. And thus clear surface evolution can be detected on two different facets. Thus the surface structure can be revealed.

1.6 Motivations of the Thesis

Zeolites and many other microporous materials are great important in industrial processes. A better understanding for their structure and growth behavior is crucial for controlling the crystal size, mophorology and properties as catalysts. Comparing with conventional methods of zeolite study, investigation of zeolite growth from their surface information is a relatively novel method. Consequently, combination of conventional study methods with AFM surface detection is expected for better understanding of the zeolite growth. The motivations of using AFM as major tool to study zeolite growth are following:

Microstructure of zeolite has not been observed directly from their morphology image with other characterization tools. As a high resolution technique, AFM could detect surface structure at nanometer, which makes it a powerful tool to observe growth behavior in detail. Surface structures and morphology characteristics of some zeolite have not been studied, limited by the single crystal synthesis. ZSM-11, whose single crystal has not been well studied, was prepared in hydrothermal method. By using AFM on ZSM-11 single crystal surface, growing feature can be shown in high resolution and growth mechanism of the surface thus can be studies. With characterization by different techniques like XRD, NMR, SEM, it is possible to monitor the crystallization.

As important catalysts, SAPO-based materials have attracted much attention. To better understand their surface properties, AFM characterization was carried out on two common used materials, SAPO-34 and SAPO-37. AFM images provide surface useful information to study the growth behavior of crystal external shape. [31,35] In addition, one of the high silicate materials, ZSM-39 was characterized by AFM and the surface morphology shows its preference in face growing.

With the use of AFM, it is possible to better understand the detailed surface structure and traces of crystallization. Thus make us be able to control the synthesis of microporous material.

1.7 References

(1) Cronsted, A. F. *Akad. Handl.* **1756**, *17*, 20.

(2) H. de St Claire Deville *Compt. Rend. Se´ances Acad. Sci.* **1862**, *54*, 324.

(3) Rees, L. V. C. *Biographical Memoirs of Fellows of the Royal Society* **1998**, *44*, 37.

(4) Breck, D. W.; Eversole, W. G.; Milton, R. M.; Reed, T. B.; Thomas, T. L. *J. Am. Chem. Soc.* **1956**, *78*, 5963.

(5) Barrer, R. M.; Stuart, W. I. *Proceedings of the Royal Society of London Series a-Mathematical and Physical Sciences* **1959**, *249*, 464.

(6) Wilson, S. T.; Lok, B. M.; Messina, C. A.; Cannan, T. R.; Flanigen, E. M. *J. Am. Chem. Soc.* **1982**, *104*, 1146.

(7) Sastre, G.; Lewis, D. W.; Catlow, C. R. A. *J. Phys. Chem. B* **1997**, *101*, 5249.

(8) Meza, L. I.; Anderson, M. W.; Agger, J. R. *Chem. Commun.* **2007**, 2473.

(9) Auerbach, S. M.; Carrado, K. A.; Dutta, P. K. *Handbook of Zeolite Science and Technology*; M. Dekker, **2003**.

(10) Pablo Cubillas, M. W. A. *Zeolites and Catalysis: Synthesis, Reactions and Applications* **2010**, Wiley.

(11) Wright, P. A. *Micropourous Framework Solids*; Royal Society of Chemistry **2008**.

(12) Corma, A.; Rey, F.; Rius, J.; Sabater, M. J.; Valencia, S. *Nature* **2004**, *431*, 287.

(13) Marchese, L.; Frache, A.; Gianotti, E.; Martra, G.; Causà, M.; Coluccia, S. *Microporous Mesoporous Mater.* **1999**, *30*, 145.

(14) Kossel, W. *Annal. Phys* **1934**, *21*, 457.

(15) Frank, F. C. *Disscuss. Faraday Soc.* **1949**, *5*, 48.

(16) Lennard-Jones, J. E. *Proc. R. Soc. Lond. A* **1924**, *106*, 463.

(17) Komiyama, M., Yashima, T. *Jpn. J. Appl. Phys.* **1994**, *33*, 3761.

(18) Komiyama, M., Tsujimichi, K., Oumi, Y., Kubo, M., and Miyamoto, A. *Appl. Surf. Sci.,* **1997**, *121-122*.

(19) Anderson, M. W.; Agger, J. R.; Thornton, J. T.; Forsyth, N. *Angew. Chem. Int. Ed.* **1996**, *35*, 1210.

(20) Agger, J. R.; Pervaiz, N.; Cheetham, A. K.; Anderson, M. W. *J. Am. Chem. Soc.* **1998**, *120*, 10754.

(21) Ono, S. S.; Matsuoka, O.; Yamamoto, S. *Microporous Mesoporous Mater.* **2001**, *48*, 103.

(22) Anderson, M. W.; Agger, J. R.; Meza, L. I.; Chong, C. B.; Cundy, C. S. *Faraday Discuss. R. Soc. Chem.* **2007**, *136*, 143.

(23) Wakihara, T.; Sugiyama, A.; Okubo, T. *Microporous Mesoporous Mater.* **2004**, *70*, 7.

(24) Agger, J. R. a. A., M.W. *Impact of Zeolites and Other Porous Materials on the New Technologies at the Beginning of the New Millennium, Parts A and B* **2002**, 93.

(25) Brent, R.; Anderson, M. W. *Angew. Chem. Int. Ed.* **2008**, *47*, 5327.

(26) Walker, A. M.; Slater, B.; Gale, J. D.; Wright, K. *Nat. Mater.* **2004**, *3*, 715.

(27) Zhang, L.; Bates, J.; Chen, D.; Nie, H.-Y.; Huang, Y. *J. Phys. Chem. C* **2011**, *115*, 22309.

(28) Holme, B.; Cubillas, P.; Cavka, J. H.; Slater, B.; Anderson, M. W.; Akporiaye, D. *Cryst. Growth Des.* **2010**, *10*, 2824.

(29) Cubillas, P.; Holden, M. A.; Anderson, M. W. *Cryst. Growth Des.* **2011**, *11*, 3163.

(30) Moh, P. Y.; Cubillas, P.; Anderson, M. W.; Attfield, M. P. *J. Am. Chem. Soc.* **2011**, *133*, 13304.

(31) Cubillas, P.; Stevens, S. M.; Blake, N.; Umemura, A.; Chong, C. B.; Terasaki, O.; Anderson, M. W. *J. Phys. Chem. C* **2011**, *115*, 12567.

(32) Putman, C. A. J.; Van der Werf, K. O.; De Grooth, B. G.; Van Hulst, N. F.; Greve, J. *Appl. Phys. Lett.* **1994**, *64*, 2454.

(33) Itzel Meza, L.; Anderson, M. W.; Slater, B.; Agger, J. R. *Phys. Chem. Chem. Phys.* **2008**, *10*, 5066.

(34) Yamamoto, S.; Sugiyama, S.; Matsuoka, O.; Kohmura, K.; Honda, T.; Banno, Y.; Nozoye, H. *J. Phys. Chem.* **1996**, *100*, 18474.

(35) Morales, J.; Astilleros, J. M.; Fernández-Díaz, L. *Cryst. Growth Des.* **2011**, *12*, 414.

Chapter 2 Experimental

2.1 Zeolite Sample Preparation

There are two main synthesis methods, hydrothermal synthesis (HTS) and Dry Gel Conversion (DGC), used to prepare the zeolite samples in this thesis [1-4]. HTS is a traditional synthesis method for zeolite preparing. A new synthesis system called dry gel conversion in which liquid solvent is much less used than HTS is also employed in our study for SAPO-34 and SAPO-37 [5,6].

2.1.1 Hydrothermal synthesis (HTS)

As mentioned, HTS is one of the most common ways for zeolite synthesis. The reaction is usually happened in a thick-walled steel vessel called autoclave (as shown in Figure 2.1), in which reacting elements are supplying along with water. The vessel must withstand the high reacting temperature for zeolite growth as well as the high pressure autogenously produced from the reaction liquid. Therefore the closure of the autoclave is a crucial property. The materials of autoclave have to be inert to the reaction. In our experiments for zeolite preparing, thus a Teflon-lined autoclave is used for the consideration for both the closure and as inert material.

A typical procedure of hydro thermal synthesis starts with a well mixing of all reaction reagents including structure building elements (commonly Si and Al for zeolites), structure directing agent (SDA), and water. The mixed hydro-gel is then kept into a hermetically sealed autoclave in an oven at certain heating temperature. After certain reaction time, the autoclave was taken out of the oven and quenched into cold water. Due to the quenching, the high temperature system in the autoclave was cooled down as well as the high-pressure reduced off. The reaction product then was taken out of the autoclave and separated into two parts for comparison. Part A was dried into air directly thus kept the entire product from the reaction, while part B was washed with distilled water for many times to clean debut and amorphous structures other than crystal.

2.1.2 Dry gel conversion (DGC)

DGC is a relatively new method for zeolite synthesis which was not reported until 1990 by Wenxiang Xu's group for synthesis of zeolite ZSM-5 [4]. It was reported that smaller sized crystals with uniformed morphology can be synthesized under DGC. Different from HTC, zeolite crystals can form under DGC without bulk water in reaction, thus the mechanism is believed as solid-to-solid transferring. A Teflon made dry gel holder is placed in the autoclave as shown in Figure 2.1 (b). Prior to heating, a small amount of water is added at the bottom of the Teflon cup.

In this thesis, the material we made with DGC is SAPO-34 and the procedure of dry gel preparation is as following: according to the composite of the gel, an appropriate amount of aluminum hydroxide was dissolved into distilled water and stirred at room temperature for 30 min. Phosphoric acid and template were then added and stirred until homogenous. The mixture was heated at 80 ˚C with continuous stirring until it turned into white solid dry gel. This pre-dried gel was ground into powder and ready for following steps of reaction in autoclave.

After specific heating time, the autoclave was taken out of the oven and quenched into cold water to stop the reaction. Similar to post-treatment in HTS, solid product in each of the autoclave was divided into two parts. One of the parts was dried in air directly and the other was wash with distilled water in a beaker and dried in the same beaker with the liquid phase. The powder dried in air was then sealed in glass vials for further analysis.

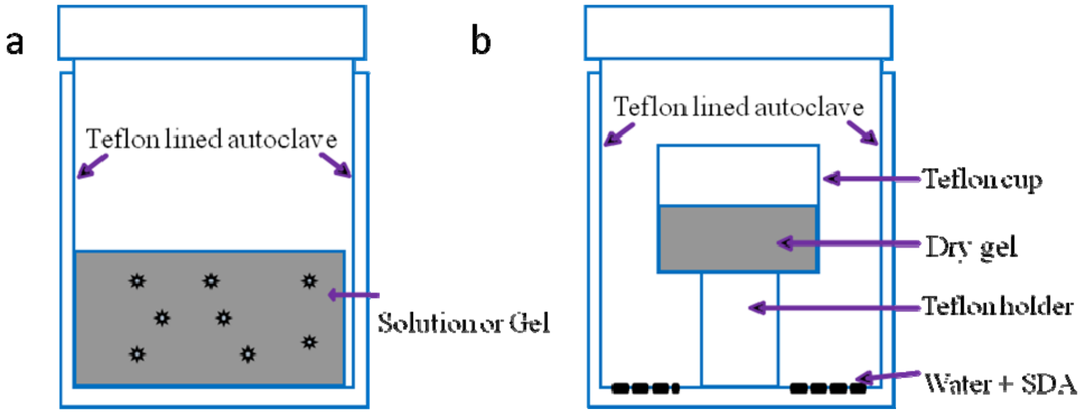

Figure 2.1 Illustration of reaction system of (a) hydrothermal synthesis (HTS), (b) dry gel conversion [7].

2.2 Characterization Methods

A variety of techniques have been used in the studies of zeolites to obtain their information and properties. Each of the techniques may only provide certain aspect of the information. Thus, a combination of different analytic techniques is necessary for a comprehensive understanding. Here in this thesis, we employ several characterization methods for zeolites study including powder X-ray diffraction (XRD), scanning electron microscopy (SEM), Atomic Force Microscopy (AFM) and solid-state nuclear magnetic resonance (SSNMR). Their fundamental principle will be briefly summarized respectively in the following.

2.2.1 Powder x-ray diffraction (XRD)

XRD is a traditional technique for crystal characterization by examining the long-range ordering and phase purity. The periodicity of the electron density in a crystal structure generates X-ray scattering from electrons and cause coherent “diffraction pattern”. The intensity of the diffracted X-ray could be plotted along with the angle 2θ (θ is the angle of electron and the crystal plane) and thus depict the powder diffraction pattern. Peaks appear in the powder diffraction pattern at the angles with maximum interference at which satisfied the Bragg’s Law [8]:

$$n \lambda = 2 d \sin \theta$$

Each framework structure has a unique diffraction pattern with characteristic peaks and relative intensity. The XRD patterns of known structures are collected in the online database (http://www.iza-online.org) of the International Zeolite Association (IZA). Therefore, one can compare the experimental XRD pattern with the standard pattern to identify the sample structure.

In this thesis, all XRD patterns were obtained between 5 to 65 on a Rigaku Rotating Anode diffract meter (45kv/160 ma) using Co $K\alpha$ radiation (λ=1.7902 Å) with 10° per minute.

2.2.2 Scanning electron microscopy (SEM)

SEM images were collected in the Nanofab at the University of Western Ontario using the Leo-Zesis 1530XB FIB/SEM Crossbeam. The crossbeam combines a high resolution SEM for imaging with a focused ion beam (FIB) for micromachining by sputter milling with a sub-100 nm lateral resolution. The spatial resolution of the images can focus down to 1 nm depending on the materials.

2.2.3 Atomic force microscopy (AFM)

AFM used in surface structure study is a Park Systems XE-100. A cantilever with nominal spring constant of 40 N/m, resonant frequency of 300 kHz and tip radius of 10 nm (NSC15, Mikro Masch) was operated under the dynamic force mode [9]. In this mode, the cantilever is vibrated at around the resonant frequency and its amplitude reduces when the tip is in proximity with the sample surface caused by the tip - sample interaction. Reduced amplitude is set as the feedback parameter (set point) so that the AFM system scans the surface contour of the sample with minimized error signals (the difference between the set point and the amplitude measured) by adjusting the distance between the tip and the sample surface.

Mapping of this distance constructs topographic image for the surface morphology. Mapping the error signal results in an image removing the height contribution and stressing only the shape of surface features. When the height range is large, surface features with small height differences are obscured. In this case, it is advantageous to use the error signal image to show the shapes of surface features, while using the topographic image to estimate the height distribution.

The scan rate for obtaining images in an area of 45×45 μm^2 is 0.5 Hz and for the images in an area of 10×10 μm^2 the rate is 1 Hz. The experiment was conducted in air with a relative humidity of ~40%.

As a canning probe detection tool with mechanical contact, AFM is a technique for materials with large flat surfaces. For most zeolites, however, final products out of synthesis are crystal powders with a large range of sizes. Therefore, the preparation of zeolites sample is a crucial process for zeolite study under AFM detection. Figure 4 shows the method we use in this study for AFM sample preparation. Firstly, we paste a sticky carbon tape on a steel substrate which could be located on the magnetic sample stage. Then disperse a small amount of sample powder onto the sticky carbon tape and blow the sample surface with pressure air to make sure crystals sticky firmly on the tape. Then the sample is ready to be used in the AFM detection.

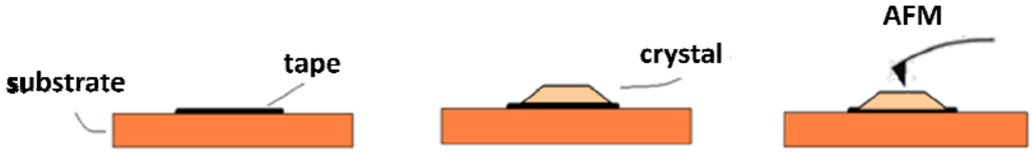

Figure 2.2 Illustration of preparation process of Zeolite sample for AFM.

2.3 References

(1) Matsukata, M., Ogura, M., Osaki, T., Hari Prasad Rao,P. R., Nomura, M. and Kikuchi, E., *Top. Catal.* **1999**, *9*, 77.

(2) Cundy, C. S. a. C., P. A *Chem. Rev.* **2003**, *103*, 663.

(3) Pablo Cubillas, M. W. A. *Zeolites and Catalysis: Synthesis, Reactions and Applications* **2010**, Wiley.

(4) Xu, W.; Dong, J.; Li, J.; Li, J.; Wu, F. *Chem. Commun.* **1990**, 755.

(5) Yang, H.; Liu, Z.; Gao, H.; Xie, Z. *J. Mater. Chem.* **2010**, *20*, 3227.

(6) Maistriau, L.; Dumont, N.; Nagy, J. B.; Gabelica, Z.; Derouane, E. G. *Zeolites* **1990**, *10*, 243.

(7) Zhang, L.; Bates, J.; Chen, D.; Nie, H.-Y.; Huang, Y. *J. Phys. Chem. C* **2011**, *115*, 22309.

(8) Bragg, W. L. *Proc. R. Soc.* **1913**, *89A*, 248.

(9) Garcia, R.; Perez, R. *Surf. Sci. Rep.* **2002**, *47*, 197.

Chapter 3 An Investigation of Crystal Growth of Zeolite ZSM-11

3.1 Introduction

Zeolite ZSM-11 is a siliceous zeolite belonging to pentasil family. Its framework structure is closely related to ZSM-5, one of the most widely used catalysts in industry [1-3]. Although we mainly focus the study on ZSM-11 in this chapter, it is helpful to introduce these two pentasil zeolites together. The first synthesis of ZSM-5 (structure type MFI) was reported by Argauer and Landolt in 1972 [3], and ZSM-11 (MEL) was first prepared by Kokotailo et al. in 1978 with tetrabutylammonium (TBA) as the structure directing agent (SDA) [4]. It soon became apparent that the material made by TBA-mediated synthesis was actually a ZSM-5/ZSM-11 intergrowth [5,6]. Phase-pure ZSM-11 was not successfully prepared until Nakagawa developed the approach utilizing 3, 5-dimethylpiperidimium derivatives as the SDAs in 1994 [7]. The excellent shape selectivity of pentasil zeolites makes them attractive candidates for commercial catalysts. ZSM-5 exhibits a high selectivity at conversion of methanol to high quality gasoline. It has also been used in many processes of oil refinery [3]. Although ZSM-11 has not been used extensively in industry yet, its catalytic properties have been well studies [8-10].

As solid catalysts, the properties of zeolites are governed by the pore sizes and the nature of cavities. In order to explore the catalytic mechanisms and optimize their performances in catalysis, it is very important to understand the details of the framework structures. Fortunately, the structural characteristics of pentasil zeolites have been well investigated [4,11,12]. Both the structures of ZSM-5 and ZSM-11 are composed of pentasil units. Different from the previously found structural units like double 4-, 6-rings in LTA or FAU topology, a pentasil unit is made up of eight 5-membered rings where Al and Si atoms locate on vertices with O atoms bonding in between (Figure 3. 1 a, oxygen atoms are not shown for clarity). Connecting to each other in one dimension, pentasil units form a linear structure called pentasil chain (Figure 3. 1 b). The pentasil chains then join through edges to form sheets with 10 membered rings (Figure 3. 2). Similar to the pentasil unit, a 10-membered ring has Al or Si atoms as vertices with O atoms in the middle of the edges. These sheets are stacked into 3-dimensional structure with 10-membered channels running through.

The structures of ZSM-11 and ZSM-5 differ in the symmetric modes of the pentasil chains. ZSM-11 has pentasil chains related to each other by mirror planes (Figure 3. 2a), its intersecting channels in both *a* and *b* direction are straight (Figure 3. 3a). Chains in ZSM-5 system however, connect to each other across the inversion centers (Figure 3. 2b). Such arrangement results in two different intersecting channels: those channels along *b* axis are straight with circular cross-section, and those channels parallel to *a* are sinusoidal with elliptical cross-section (Figure 3. 3b) [12].

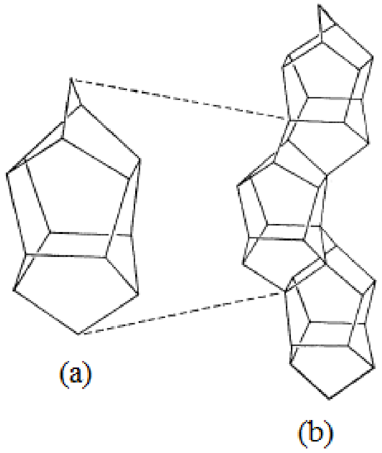

Figure 3. 1 Illustration of pentasil zeolite units (a) and pentasil Chain (b). Oxygen atoms locating at the middle of all bonds are not shown for clarity [3].

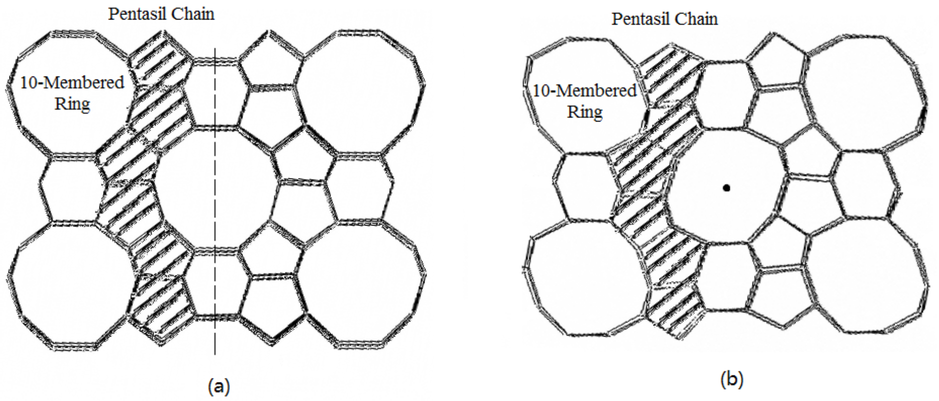

Figure 3. 2 Illustration of pentasil sheet structures. (a) structure of ZSM-11, pentasil chains relate to each other by mirror symmetry, (b) structure of ZSM-5, pentasil chains connect to each other across the inverse center [12].

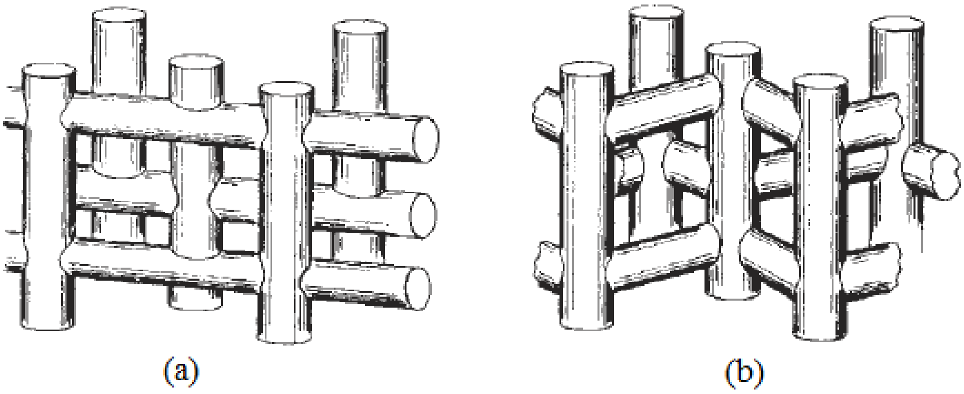

Figure 3. 3 Illustration of intersecting channel structure. (a) Channel structure of ZSM-11, channels are straight in both *a* and *b* direction [4]; (b) channel structure of ZSM-5, channels are straight along *b* axis and sinusoidal along *a* axis [3].

To better control the crystal size, morphology and surface properties for different applications, it is important to understand the growth behavior of zeolites. Due to the difficulties in phase pure synthesis of ZSM-11, however, not too many studies have been focused on its crystallization processes. Therefore, it is important to choose a proper synthesis method to study the nucleation and crystal growth. Among several synthetic methods, HTS is a very reliable approach to obtain high quality zeolites since it can provide stable conditions for nucleation and crystal growth. On the other hand, HTS is a very complicated process which relates crystal growth to a number of factors and equilibriums in both liquid and solid phases. In some reported studies, in-situ observation of crystallization provided key information on the crystal growth of some zeolites [13,14]. However, experimental vessels for in-situ studies usually need to be specially designed to withstand the high temperature and high pressure environments, and it is even harder to integrate such vessel with spectroscopic techniques for in-situ study. Consequently, crystallization is often studied by ex-situ approach. This method involves quenching reactions at different heating times to obtain solid intermediates at different crystalline stages [15,16]. The obtained solid samples in different reacting times then are characterized by different analytical techniques.

In this chapter, the crystal growth behavior of zeolite ZSM-11 is investigated by preparing a series of intermediates in different reaction times under HTS conditions. These intermediates are then characterized by different spectroscopic methods. As a conventional technique for structural studies, powder X-ray diffraction (P-XRD) is used to monitor the evolution of long range ordering of the samples as a function of crystallization time. Solid-State NMR (SSNMR) is employed for short-range structural analysis. In this study, we use ^{29}Si, ^{13}C, ^{19}F SSNMR to follow changes in the local environments of Si atoms, to probe the behavior of SDA, and to identify F^- species. SEM is also utilized to characterize the sample morphology in micro scale level. AFM provided high-resolution images that help to reveal the relationship between the surface morphology and the framework structure. Most of the reported ZSM-11 synthesis methods can only produce crystals with either very small size or irregular morphologies [5,9,17-19], which makes it hard for detailed surface characterization using AFM. With HTS method using *N, N*-dipropylhexamethyleneiminium (DPHMII) as SDA and NH_4F as mineralizing agent [20], we successfully prepared ZSM-11 single crystal in large sizes. These crystals exhibit typical morphology of tetragonal system. They have good surface conditions suitable for AFM analysis. By careful examining the AFM images, detailed growing features on both (110) and (111) faces are observed in micro scale for the first time. By studying the framework structure, the growing features are correlated accurately to the structural units. The combination of AFM, XRD, SEM, and NMR results allows one to obtain a clear picture of the crystallization process and morphology evolution of ZSM-11.

3.2 Experimental Details

3.2.1 Sample preparation

ZSM-11 intermediate samples were synthesized by ex-situ HTS method [20]. The silicon source was colloidal silica (LUDOX Am-30, Sigma-Aldrich) suspension in water. *N, N*-dipropylhexamethyleneiminium iodide (DPHMII) was used as SDA. Ammonium fluoride (98%, Alfa Aesar) was utilized as a mineralizing agent, and the remainder was distilled water. The initial composite molar ratio was $1.0SiO_2$: $0.4NH_4F$: 0.056DPHMII: $4.2H_2O$. A typical procedure for HTS synthesis is following: 3.0 g NH_4F, 0.84 g DPHMII, and 6.7 g colloidal silica were mixed with 1.3 g H_2O in a 50 ml Teflon cup. The mixture was stirred intensively at room temperature for 10 min for homogeneity. The Teflon cup was then sealed inside a steel autoclave. A series of intermediates were synthesized by preparing several initial gels with the same composition. The autoclaves were then kept in an oven at a temperature at 170 ˚C. At different heating times, the autoclaves were taken out of the oven and quenched in cold water to stop the reactions. Liquid phase in each autoclave was separated from solid phase by centrifugation and kept as mother liquor. The solid phase was then separated into two parts; part A was dried in air at room temperature and part B was well washed with distilled water to remove impurities.

Synthesized crystals could obtain more surface features with a re-growing treatment. Thus the growth behavior in diluted solution can be investigated [14]. For ZSM-11 crystals, this treatment includes putting prepared large crystals back in diluted mother liquor and heating in oven for certain time. In practical, 0.5 g ZSM-11 crystals were put in the Teflon cup with 19 ml (95%) ethanol and 1 ml (5%) mother liquor collected from former HTS synthesis. The Teflon cup was then placed into an autoclave and kept in oven at 170˚C. After heating for different times the autoclaves were quenched in cold water, and the re-grown crystal samples were separated from the re-growth solution.

The template DPHMII (structure shows in Figure 3. 4) was synthesized using a literature method [21]. At first, 25 g hexamethyleneimine (Sigma-aldrich) and 35 g potassium bicarbonate ($KHCO_3$) (Alfa Aesar) were added into a round bottom flask containing 200ml methanol. The resulting mixture was stirred inside the round bottom flask that was submerged in an oil bath that was kept at a temperature of 50 °C. Then, 70 ml of 1-iodopropane was added drop-wise into the reaction mixture. The mixture was allowed to react for 48 hours until a dark brown liquid and white powder precipitate were obtained. The mixture was then rotary evaporated to remove the methanol and the solid part obtained was dissolved into chloroform to separate the crude DPHMII from solid $KHCO_3$. Chloroform was then removed from the solution by rotary evaporation, and the solid obtained at this step is the crude DPHMII. The solid was re-crystallized in methanol/2-propanol mixture. If the re-crystallized sample still has a light yellow appearance, it is then washed in excess ethyl acetate until the powder is completely white.

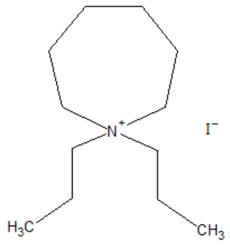

Figure 3. 4 Molecular structure of N, N- dipropylhexamethyleneiminium (DPHMII).

3.2.2 Characterization

Powder XRD patterns of the intermediates were obtained on a Rigaku diffractometer with Co Kα radiation (λ=1.7902 Å). SEM analysis was performed on LEO 1530 Field Emission Scanning Electron Microscope, and for each sample a 3 nm osmium layer was coated using a Filgen OPC-80T instrument.

AFM used in surface structure study is a Park Systems XE-100. A cantilever with nominal spring constant of 40 N/m, resonant frequency of 300 kHz and tip radius of 10 nm (NSC15, Mikro Masch) was operated under the dynamic force mode. In this mode, the cantilever is vibrated at around the resonant frequency and its amplitude reduces when the tip is in proximity with the sample surface caused by the tip - sample interaction. Reduced amplitude is set as the feedback parameter (set point) so that the AFM system scans the surface contour of the sample with minimized error signals (the difference between the set point and the amplitude measured) by adjusting the distance between the tip and the sample surface. Mapping of this distance constructs topographic image for the surface morphology. Mapping the error signal results in an image removing the height contribution and stressing only the shape of surface features. When the height range is large, surface features with small height differences are obscured. In this case, it is advantageous to use the error signal image to show the shapes of surface features, while using the topographic image to estimate the height distribution. The scan rate for obtaining images in an area of $45\times45\ \mu m^2$ is 0.5 Hz and for the images in an area of $10\times10\ \mu m^2$ the rate is 1 Hz. The experiment was conducted in air with a relative humidity of ~40%.

All the NMR experiments were carried out on a Varian/Chemagnetics Infinityplus 400 WB spectrometer equipped with three reference channels operating at the field strength of 9.4 T. The Larmor frequencies of ^1H, ^{13}C, ^{29}Si and ^{19}F were 399.5, 100.4, 79.4, and 375.9 MHz, respectively. The magic angle was set by using the ^{79}Br resonance of KBr. The chemical shifts of ^{13}C, ^{29}Si, and ^{19}F were referenced to adamantine, tetrakis(trimethylsilyl)-silane (TTMSS), and trifluorotoluene, respectively. Depending on the requirements of the individual experiment, we used two NMR probes (Varian/Chemagnetics 9.0-mm and 4.0-mm H/X/Y triple-tuned T3 MAS probe). The ^{19}F MAS spectra were obtained by using 4.0-mm probe A 30° pulse was used with a pulse delay of 10 s. For each sample, ^{19}F spectra at 10 and 12 kHz spinning speeds were both recorded to determine the isotropic peaks from the sidebands. For the ^{29}Si MAS experiments, a 9.0 mm probe was used with a 30° pulse and a pulse delay of 30 s. For $^1H \rightarrow {}^{29}Si$ cross-polarization (CP) experiments, the ^1H 90° pulse length was 9.5 μs. A contact time of 0.5 ms and the pulse delay of 10 s were used. The ^{13}C CP MAS spectra were recorded by using the 4.0 mm probe with a contact time of 2 ms and a pulse delay of 10 s.

3.3 Results and Discussion

3.3.1 XRD results

Powder X-ray diffraction was used to study the evolution of long-rang ordering in ZSM-11 intermediates, and the selected patterns are shown in Figure 3. 5a. The pattern of 2-day (2d) sample presents a very broad peak, which indicates that the sample is amorphous materials without long-range ordering. This specifies that no crystalline structures have been formed after 2 days of hydrothermal treatment, and the solids in reaction are amorphous materials. Heating the samples for 3 days led to the emergence of several peaks whose position correspond to (200), (501), and (10 00) reflections belonging to ZSM-11. These peaks demonstrate the beginning of the crystallization under the influence of SDA. The broad amorphous peak still presents indicating that the sample contains a significant amount of the amorphous materials. This stage can be identified as early stage of the crystallization. After 4 days, more characteristic reflections akin to the ZSM-11 structure begin to appear, and the sharp peaks existing in 3d, 4d patterns keep increasing the intensities, and more characteristic peaks keep showing. In contrast, the intensity of the broad peak due to amorphous materials decreases. Further heating the reaction results continuous increase in the intensity of the peaks due to ZSM-11 and disappearing of the broad reflection belonging to the amorphous materials. The XRD pattern of 6d sample only contains the peak due to ZSM-11, it is indicative that the crystallization is complete. All diffraction peaks of 7 day sample can be assigned to the *hkl* reflections of ZSM-11 crystal structure (standard XRD pattern of ZSM-11 was referred from IZA, not showing) [12]. During the crystallization, the peaks showing in each stage all belong to ZSM-11, which implies that no other crystalline phase is formed during crystallization

To examine the species that may be affected upon the washing treatment, the XRD patterns of unwashed samples are shown in Figure 3. 5b. The labeled reflections correspond to the position of crystal of DPHMII pattern, the SDA. It is indicative that DPHMII at the early stage was in liquid phase rather than involved in gel formation. And the DSA is re-crystallized upon drying. Other peaks are not able to be classified in any structure known, but they represent the nutrient components in the growth solution. XRD patterns for longer reaction time are very similar to washed samples without reflections of crystal DPHMII, which demonstrate the SDA's incorporation in framework structure.

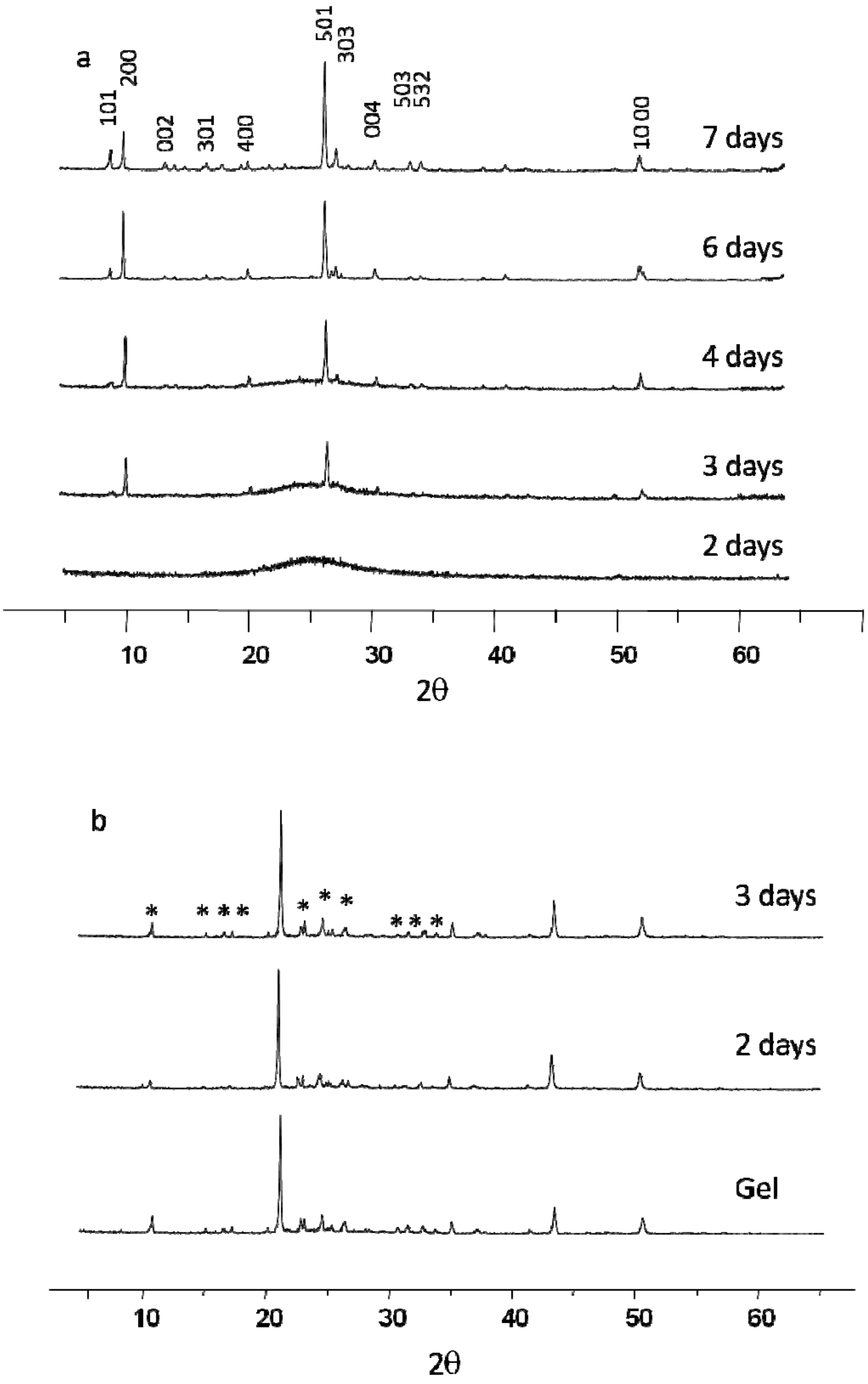

Figure 3. 5 XRD patterns for ZSM-11 prepared with different reaction times. (a) Pattern of washed samples, (b) patterns of unwashed samples.

3.3.2 NMR results

To further investigate the changes in the local environments of Si atoms, ^{29}Si MAS and ^{1}H → ^{29}Si CP MAS spectra were obtained and are shown in Figures 3. 6. All ^{29}Si MAS spectra from initial gel to 7d sample present a strong peak at around -113 ppm, which can be assigned to the Q^4 silicon atoms (silicon atoms connected to four other silicon by oxygen) [22,23]. According to the XRD pattern, the 2d sample mainly contains amorphous materials at the beginning of the reaction. Therefore, the Q^4 peak in gel and 2d NMR spectra corresponds to the silicon atoms in amorphous silica species. In addition, a weak shoulder signal presents next to the major peak at around -102 ppm, which can be assigned to Q^3 silicon atoms (silicon atoms connected to three other silicon by oxygen atoms and bonded to a neighboring -OH). The Q^3 signal is due to the Si atoms bonding to the -OH group at the surface of the amorphous silica. The CP NMR experiment is a technique that utilizes the ^{1}H - ^{29}Si dipolar interaction. It can enhance the intensity of the ^{29}Si nuclides with protons in their close proximity. In the CP MAS spectra, the -102 ppm peak has high intensity due to the strong dipolar interaction between the -OH and Si in Q3 species of the amorphous particles. The Q^4 silicon, without silanol groups directly attached, also shows a weak peak. This CP signal is mainly caused by the interaction between the Q^4 silicon atoms with silanol group in amorphous materials and the protons in the SDA molecules.

The 3d and 4d XRD patterns demonstrate that ZSM-11 crystallization proceeds with consuming the amorphous materials at these times. This result is also supported by the ^{29}Si NMR spectra. The change of intensity due to Q^3 shoulder peak is not significantly noticeable in ^{29}Si MAS spectra. Nonetheless, the CP spectra clearly show that the intensity of Q^3 peak becomes lower comparing with that of the Q^4. The decrease of Q^3 intensity corresponds to the reducing of amorphous materials; and the enhancement in Q^4 peak is due to bulk silica species forming from hydrocondensation among Q^3 sites ($O_3SiOH + OH\text{-}SiO_3 \rightarrow O_3Si\text{-}O\text{-}SiO_3 + H_2O$) sites condensation in to two $Si(SiO)_4$ sties by losing a H_2O). In this way, the silicon species are rearranged from amorphous solids into crystalline structure or the crystal precursors to the crystalline product with silicon sites gathering around the SDA molecules. The Q^4 signal get enhanced at this stage, due to the increase of the number of silicon atoms in Q^4 sites interacting with the protons in the SDA molecules.

After heating the gel for 6 days or longer, the Q^3 peak in both MAS and CP MAS spectra becomes very weak. This is due to the consumption of amorphous materials during the crystallization. The CP spectra show a strong peak of Q^4. At the lacking of silanol group on amorphous materials, the enhancement is mainly due to interaction between silicon sites in the framework with the protons in the SDA molecules. This indicates that the SDA molecule locates very close to the silicon atoms in framework. In washed samples, it is most likely that the SDA molecule are located in the intersection of the 10-rings channels [24].

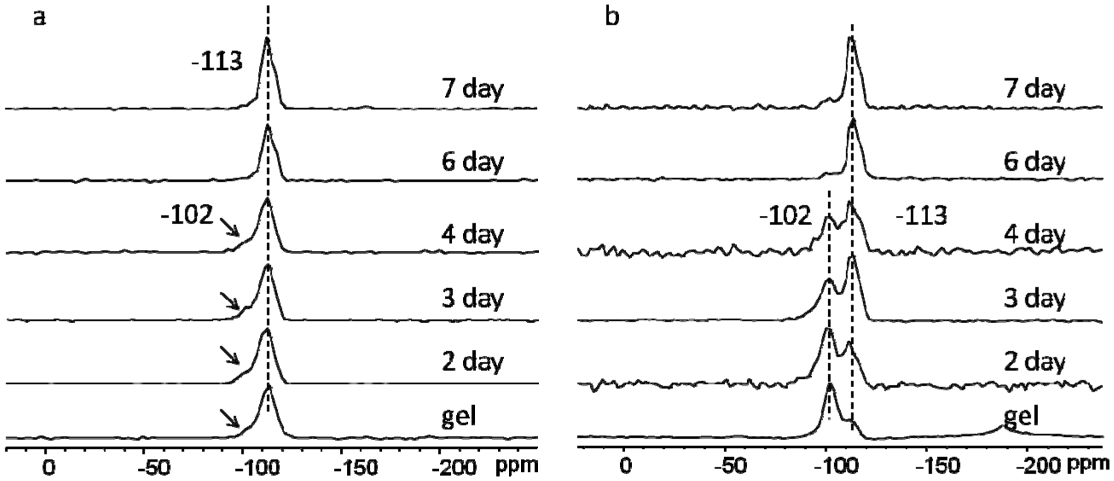

Figure 3. 6 ^{29}Si MAS (a) and ^{1}H → ^{29}Si CP spectra of selected samples with a contact time of 0.5 ms (b).

The ^{13}C CP MAS spectra of selected intermediates are obtained to follow the behavior of the SDA molecules. Peak assignments are shown in Figure 3. 7a. In the spectrum of initial gel, not all characteristic peaks are presented, and the peaks have weak intensities. This spectrum demonstrates that most of the SDA molecules have not been incorporated in the siliceous gel at the beginning of the reaction. According to the unwashed XRD pattern, most SDAs are in the reaction solution. With a longer reaction time, the 2d sample spectrum shows all the characteristic peaks and the peaks become stronger, which indicates the beginning of SDA's imparting into the siliceous gel. Strong signals appear in the samples after 3-day reaction. The strong signals verify that the SDA molecules are occluded in the channels of ZSM-11after complete crystallization.

The ^{19}F MAS spectra were recorded to examine the F^- species produced in crystallization (Figure 3. 7b). Spectra of 6d and 7d samples exhibit two isotropic peaks with associated spinning sidebands (sidebands are labeled with * or °). Both isotropic peaks were also observed in ZSM-5study of ^{19}F NMR spectra[25]. In ZSM-5, the peak around 66 ppm is in the range of F^- covalently bonded to Si atom in the framework[26]. Due to ZSM-11 has a very close structure with ZSM-5, this peak can be assigned to the F^- bonding to Si atom in Framework. For the peak at -78 ppm however, its nature has not been deduced even in ZSM-5, thus we cannot determine its chemical environments [26]. A -127 ppm peak presents with a broad background signal due to the probe[26].

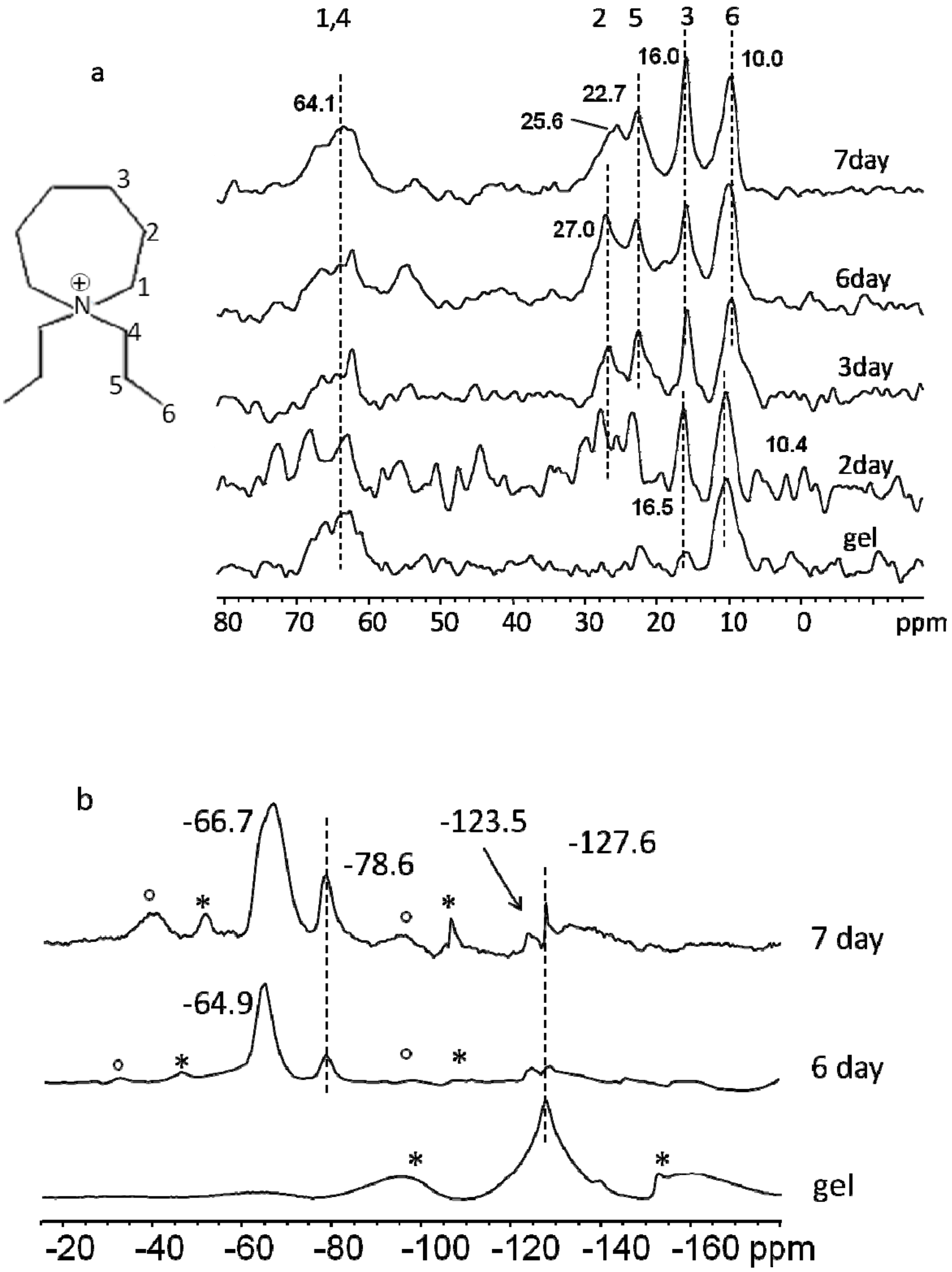

Figure 3. 7 (a) ^{13}C CP MAS spectra and (b) ^{19}F MAS spectra of selected samples.

3.3.3 SEM results

According to the XRD and NMR results, ZSM-11 crystallization involves an evolution from small-dimensional amorphous materials to crystalline structure. Through the use of SEM, it is possible to follow in detail the changes of the sample morphology in nanometer level [27,28]. The information on morphology provided by SEM is more straightforward than that offered by structural analytical methods like XRD and SSNMR. In this study, we carefully examined the intermediates by SEM and found that the samples with reaction time of 2 days, 4 days and 7 days present obvious characteristic in the micrographs.

Figure 3. 8 show scanning electron micrographs of the sample obtained after 2 days. In the overview images (Figure 3. 8a and b), the sample mainly contains solid materials without obvious regular crystal surfaces. This is consistent with the XRD results that the majority of the sample is amorphous materials in 2d reaction. Some of these amorphous solids are loosely aggregated into rounded shape. Amplified image of the amorphous aggregations (Figure 3. 8c) clearly shows a spherical structure composing of solid particles attaching to each other. The ball-shaped solid is about 500 nm in diameter and it has a very rough surface. It indicates that the growth mechanism is adhesive growth which usually takes place at high supersaturation. The detailed morphology of the amorphous solid is further examined in the amplified image shown in Figure 3. 8d. An individual particle with irregular shape located in the center of the image has a sized of 50 nm in diameter. Amorphous materials on the rest of the image are aggregated and cross-linking to each other. The SEM image indicates the non-crystalline morphology, confirming the XRD and NMR results. This reaction stage could be considered as in the early period of the zeolites synthesis. At this stage, the silica is dissolved in the solution along with hydrolysis process, and the polycondensation of silicate species take place in the reaction system. The intermediate only has short range structures. The crystalline structure has not been built and the most of the samples are amorphous.

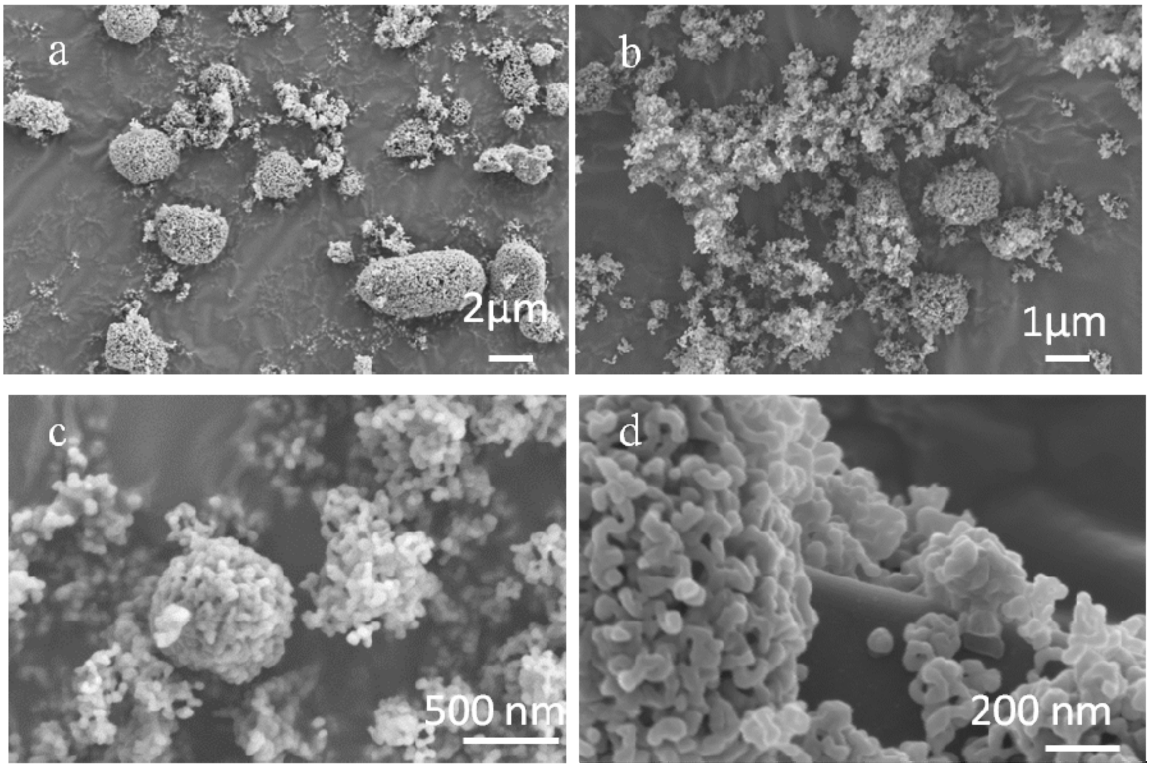

Figure 3. 8 SEM micrographs of 2 day sample. (a-b) Overview images of amorphous with aggregation, (c) amplified image of an aggregation, (d) amplified image of amorphous materials.

According to the XRD results, 4 days sample is a typical intermediate where the crystallization just starts occurring; such product contains both amorphous materials from the earlier stage and possible crystalline material with MEL structure. The SEM images of the 4d sample present with characteristic features in Figures 3. 9. The overview of the sample (Figure 3. 9a and b) shows different crystal structures mixing with amorphous materials. Careful observing notices that there are three types of regular crystal shapes: spherical crystal particles, octahedral crystals and needle-shaped crystals. The spherical crystals have sizes around 1-2 μm in diameter with rough surface. In Fig. 3. 9c, an amplified image shows a spherical crystal whose morphology and surface conditions are similar to thos of the amorphous aggregation in the earlier stage (2d). This evidently verifies that the ball-shaped crystalline structure are formed from the polycondensation of silicate species by adhesive growth mechanism [14]. Several early stage crystalline structures are shown in Fig. 3. 9d. Their sizes are comparable to those of the spherical crystals.

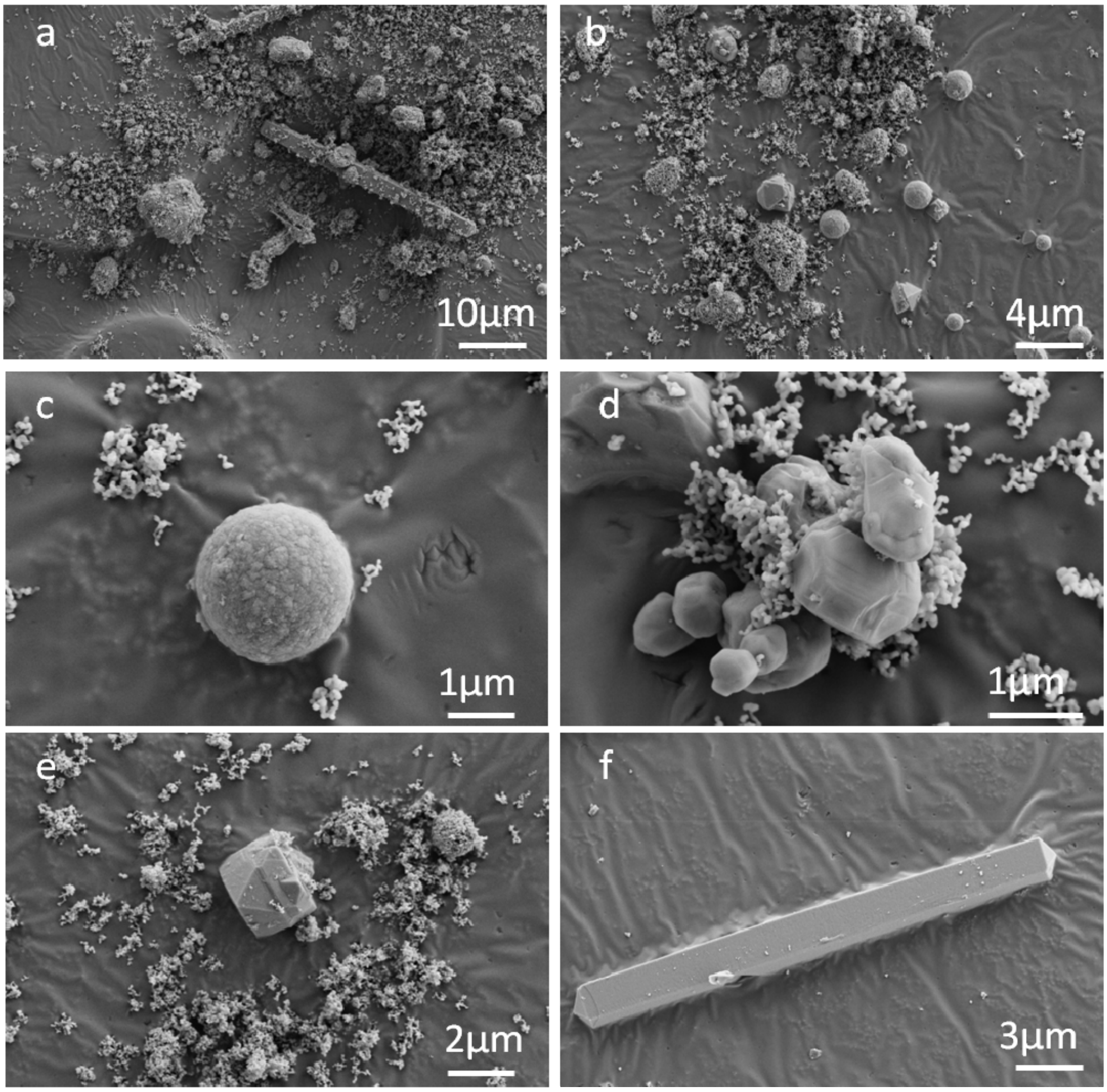

Figure 3. 9 SEM micrographs of 4-day sample (a-b) Overview image of the sample; (c) a crystal ball on carbon substrate; (c) gathered crystalline structure; (e) a crystal with octahedral morphology; (f) a typical needle-shaped crystal.

These crystals have rounded shape with smooth surfaces that could possibly develop into regular crystal faces in later cryataliztion, which is an evidence of pre-stage of the fully developed crystals [27]. Interestingly, two typical shapes of single crystal in tetragonal system, the octahedra and the needle-shapes, are both shown in this sample. The octahedral crystals present eight triangular facets (Fig. 3. 9e) with the size around 1μm on edges. Each crystal with needle-like appearance has a prism body part connected to simi-octahedral tips (Fig. 3. 9f) on both ends. The rectangular shaped faces of the prism part could be assigned to (110) face and the 4 embraced triangular faces at the tip parts could be assigned to (111), based on crystallography knowledge [29]. The crystal sizes of this type are ranged from $2\times2\times20$ μm^3 to $5\times5\times40$ μm^3. The octahedral crystals only found in the 4d sample and disappear in samples with longer reaction times. For samples heating over 6 days, the crystal only contains needle-like shape. As both of the morphologies are typical in tetragonal crystal system, two growth habits can be concluded. 1) Between the two exhibits, the needle shape is what the final crystal preferred. Therefore, the observed octahedral crystals in 4d sample possibly develop into needle shape with enlarging of the crystal sizes. 2) The octahedral morphology is a transition status that only appears at the induction time of crystallization. As the induction time of crystallization is usually very short, the octahedral morphology sample is not commonly observed in samples [30].

Figure 3. 10a and b show SEM images of ZSM-11 sample with 7-day reaction. Crystals exhibit uniform shape of tetragonal single crystals, whose sizes range from $15\times15\times80$ μm^3 to $30\times30\times120$ μm^3. The crystal size is significantly larger than the early samples, indicating that the crystals grow in size. Crystals in this sample show fine surfaces, indicating the low supersaturation in growth solution.

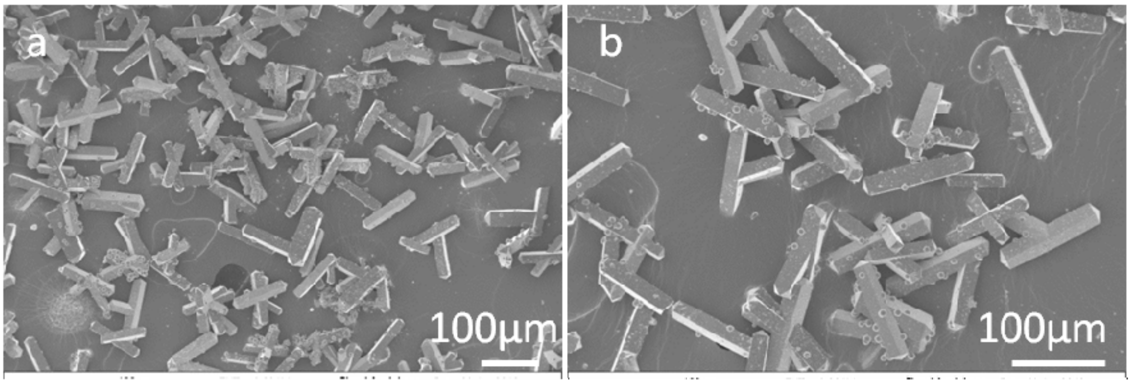

Figure 3. 10 SEM micrographs of 7-day sample. Both (a) and (b) show overview image of typical tetragonal crystals.

3.3.4 AFM results

AFM is a powerful technique for surface investigation by providing material topology in high resolution [31,32]. In recent years, AFM has been utilized to study the crystallization of microporous materials by visualizing detailed events on crystal surfaces in nanometer scale [33,34]. Formerly reported AFM study on MEL structure only show work done on intergrowth crystal [19]. Since no crystal face is assigned to its Miller-Index (MI), it is hard to reveal the relationship between the captured features and the framework structure. In this thesis, we successfully obtained ZSM-11 single crystal with typical tetragonal-system shapes under HTS conditions. So zeolite crystal surfaces can be correlated to their framework structure, which permits the investigation of the growing structure. Since surface events provide reliable information about the synthesis conditions, therefore studying these features in detail can shed light on better understanding of the zeolite crystallization.

AFM is a delicate instrument designed for scanning on small scale surface with height distribution within its capable z-direction adjustment. The image quality heavily relies on the sample surface conditions. For our study, not all the prepared samples are suitable for AFM analysis. The amorphous solids of 2d sample rarely show face structure so that the AFM images show general morphology quite similar with the SEM results. For 4d samples, the small sizes of the crystals limit the quality of the AFM images. Further, there are too many very small amorphous particles on the crystal surface, which made surface scanning particularly difficult. Therefore, only 7day samples with suitable crystal faces are able to give good AFM images providing significant structural information.

Most crystals of 7d sample present fine surfaces that provide AFM with ideal working environments. Figure 3. 11 shows error signal images of a 7d ZSM-11 crystal with needle shape. Because the topographic image has a large height range, which obscures the small scale features on the crystal, we show the error signal image for clarity. Corresponding to the crystal morphology in SEM images, the tip part (Figure 3. 11a) presents the four triangular faces embracing in a 4-fold symmetry along the crystal long edge. So the crystal shape could be simply considered as two pyramid-shaped tips connecting to a 4-fold prism. The triangular faces of the tip part can be assigned to (111) face. Figure 3. 11b shows the overview image of the prism part of the ZSM-11 crystal. It shows flat (110) face with only a few small nuclei, which is ideal crystal face for detailed analysis. The regular shapes of the crystal facets indicate that the (110) face was fully developed into a typical tetragonal single crystal.

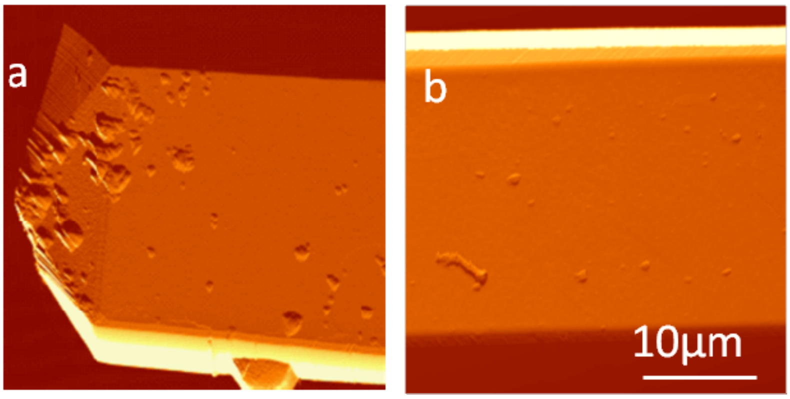

Figure 3. 11 AFM Error image of ZSM-11 (a) Tip part of the typical shaped crystal (b) (110) face on the body part.

In some AFM studies of surface structures, large sized layered structures with regular shape were observed on crystal surface, which represents the possible growth mechanism of the crystal [28,35-38]. These zeolitic systems include Zeolite A (LTA), zeolite X/Y (FAU) or zeolite L (LTL), whose framework are built up from the structural simpler units like double 4-, 6-rings. In our study of MEL structure type, however, large sized crystal layer was not found on synthesized samples, but some bulk nuclei were observed on the crystal surface. Therefore, we examined the amplified images on the flat area of the surface, searching for possible growth features in smaller scale. Figure 3. 12 show a series of AFM images that gradually zoomed-in on one position of the (110) face. Figure 3. 12a, is an overview image in size of $10\times10\mu m^2$, on which a misplacement happened at 6 μm in vertical direction due to displacement of the sample during the scanning. But to keep the position consistence of the four images, the image is still shown. In this image, a (110) face of a crystal is shown and the surface present flat plane with 10 μm in width. Figure 3. 12b was obtained by zooming in a square area on the flat surface with no obvious nuclei particles in Figure 3. 12a. In this amplified image, the former flat area becomes rougher due to more accurate scanning in smaller are. And several nuclei particles at the image margin become more obvious than they were in Figure 3. 12a. Further zooming in the area without those marginal particles, one can observe the small sized nuclei shown clearly in Figure 3. 12c. More detailed surface features on the surface become visible. To present the nuclei in the best resolution AFM can offer, Figure 3. 12d shows surface nuclei in a 1×1 μm^2. Careful observing notices that the nuclei have the uniform lateral sizes around 100 nm in diameter. Among the nuclei shown in the image, some have sharp outlines and locate on the top of the surface as isolated neclei, whereas some have blur edges merging to each other and locate among the pile. According to the nucleation behavior [30], the nuclei with sharp outline could be considered as “newly” born. The nuclei merging into the face are evidences of “spread nuclei” due to crystal growth. The nuclei on this face indicate the growth mechanism belongs to “birth and spread”, which usually happen in solution with low supersaturation.

Another advantage of AFM analysis is its ability of accurate measurement for surface feature in nanometer scale in lateral dimension and sub-nanometer scale in height. There have been many studies reported with precise height information of the surface features [18,35-37,39]. In Figure 3. 13a, two newly born nuclei with sharp outline were chosen to take the measurement. The cross-sectional profiles are shown in Figure 3. 13b. The line profiles in red and green stand for the labeled marks of red and green in Figure 3. 13a, respectively. In both of the line profiles, the nuclei are 3 nm in height and 100 nm in lateral. Therefore, the nuclei observed from the AFM image is more like a thin terrace with the area sized significantly larger of its height.

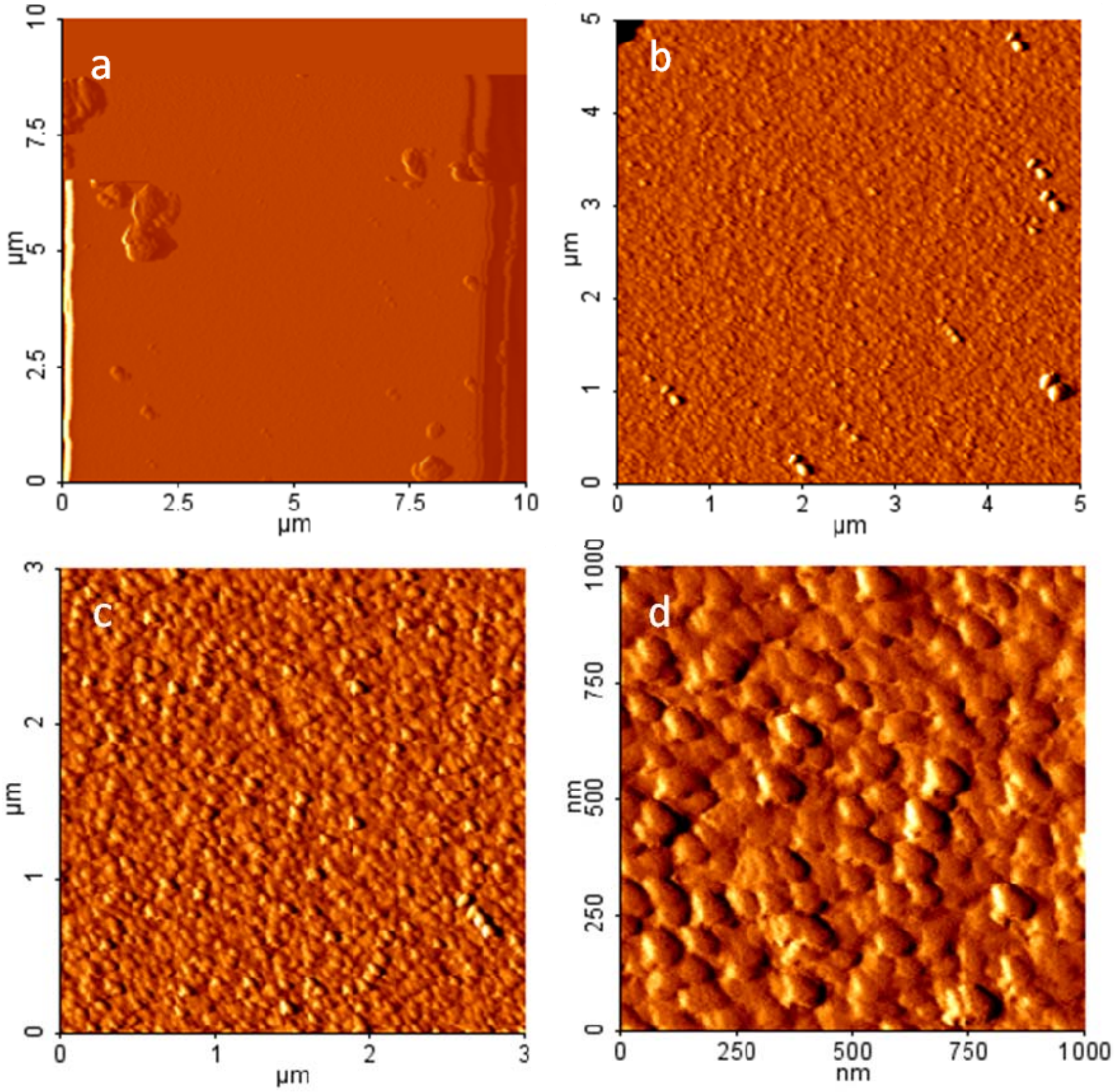

Figure 3. 12 A series zoomed-in AFM images on (110) face of ZSM-11.

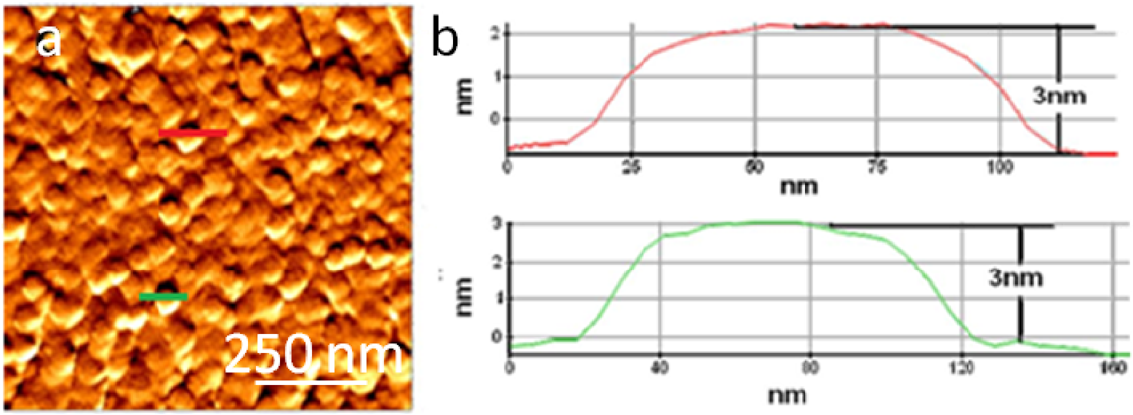

Figure 3. 13 (a) Amplified image of flat area on (001) face; (b) cross-sectional profile of red and green line on (a).

To further correlate AFM data with zeolite structure, we carefully studied the crystal structure of ZSM-11. Morphology and framework schemes of ZSM-11 are shown in Figure 3. 14a. Firstly a scheme of typical shape of tetragonal single crystal with the crystal axis is shown in Figure 3. 14a. Synthesized crystals in our study have the same morphology, accordingly, the *a*, *b* and *c* unit cell axis in crystal are along the directions shown the figure. As shown in Figure 3. 14b, the unit cell edge length of in *a* and *b* directions are 2nm, thus the diagonal of the unit cell is 2.8nm. In Figure 3. 14c, the framework projection in [001] direction (seeing along *c* axis) shows that the possible step height of the layer of unit cell on the (110) plane is 2.8 nm. AFM results show the observed nuclei heights are 2.7-3.0 nm along this direction. The 3nm-high nuclei in Figure 3. 13a correspond to the layer of unit cell structure in (110) plane. Channels in [001] and [010] directions cross by 90 degree angle in the framework structure, which is consistent to the model scheme of two-dimensional channels in Figure 3. 3a [12]. The crystal has intersect channels in direction *a* and *b*, whereas no large channel go along [001] direction.

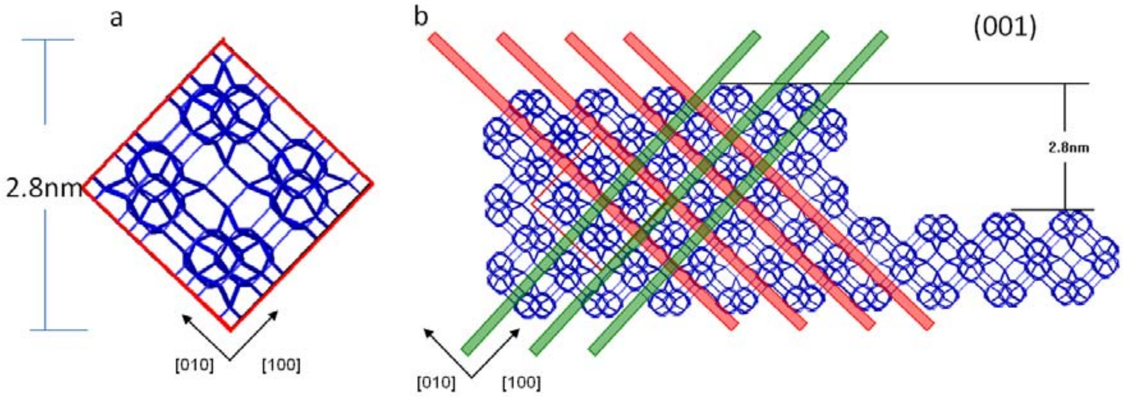

Figure 3. 14 Illustrative schemes of MEL (ZSM-11) framework structure (a) Typical crystal shape of tetragonal system; (b) unit cell structure of MEL view along *c* axis; (c) step height illustration scheme.

The crystal formation mechanism could be further investigated by combining the morphology and the structure analysis. As discussed earlier, pentasil chains are the basic building structure for crystal growth. In the simplified scheme shown in Figure 3. 15, each building unit shows in orange (or blue) consists of four pentasil chains. On the (110) face, this type building structures are lying along the *c* direction and join into nucleus. The illustrative (001) face presented in blue (at the right lower corner) corresponds to the Figure 3. 14c. The crystal shape is determined by the ratio of the growing rates of two directions. (1) The rate of the elongation of pentasil chains influences the length of crystals morphology along c direction. (2) The rate of the adhesion between the pentasil chains determines the a and b dimensional size. Due to the crystal morphology we observed, it indicates that the elongation rate of the pentasil chains is significantly faster than the adhesive growth rate. Therefore, the crystals exhibit a needle shape morphology.

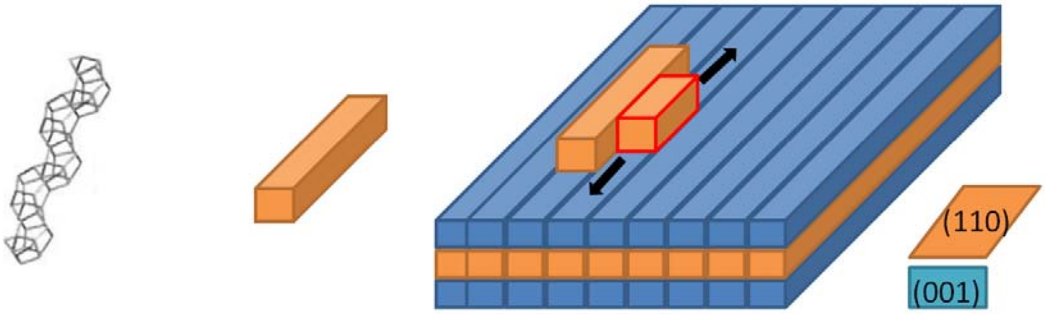

Figure 3. 15 Illustrative scheme of structure building in pentasil crystals.

In some AFM studies of porous materials, crystals are put back into solutions for re-growing [14]. By varying the re-growing conditions, one can obtain crystals with more detailed traces on the surface of substrate crystal which can be captured by AFM. In this method, the synthesized crystals perform as framework substrates, and new features take place on the crystal surfaces. In this study, we put synthesized ZSM-11 crystals back into the diluted mother liquor to examine the crystal growth behavior in low supersaturation. A series of samples (1 day, 4 h, 2 h, 1 h) were carried out for re-growing but only 1h re-growing samples show visible new features. In other samples (1 day, 4 h, 2 h), crystals put back were dissolved.

Figure 3. 16 shows (001) faces of crystal ZSM-11 after re-growing treatment. The substrate crystal gained a significant amount of large nuclei on its surface. The nuclei sizes range from 100-800 nm in lateral diameter and with height less than 100 nm. Figure 3. 16b is a zoomed-in image on Figure 3. 16a. The cross-sectional line profiles are provided to show the height of the two thinnest layered nuclei marked in red and green respectively. The cross-sectional profiles show the height of these two nuclei are 12 and 17 nm, corresponding to the height of 4 layers and 6 layers of unit cell in framework structure. Another layer structure with large lateral sized was found in Figure 3. 16e. The height of the layered nucleus is 12 nm and the lateral diagonal is around 2.5 μm. In such a large area, the layer height is homogeneously contains 4 unit cell layer height. It

consolidated that the “birth and spread” is the main growing mechanism in low supersaturation.

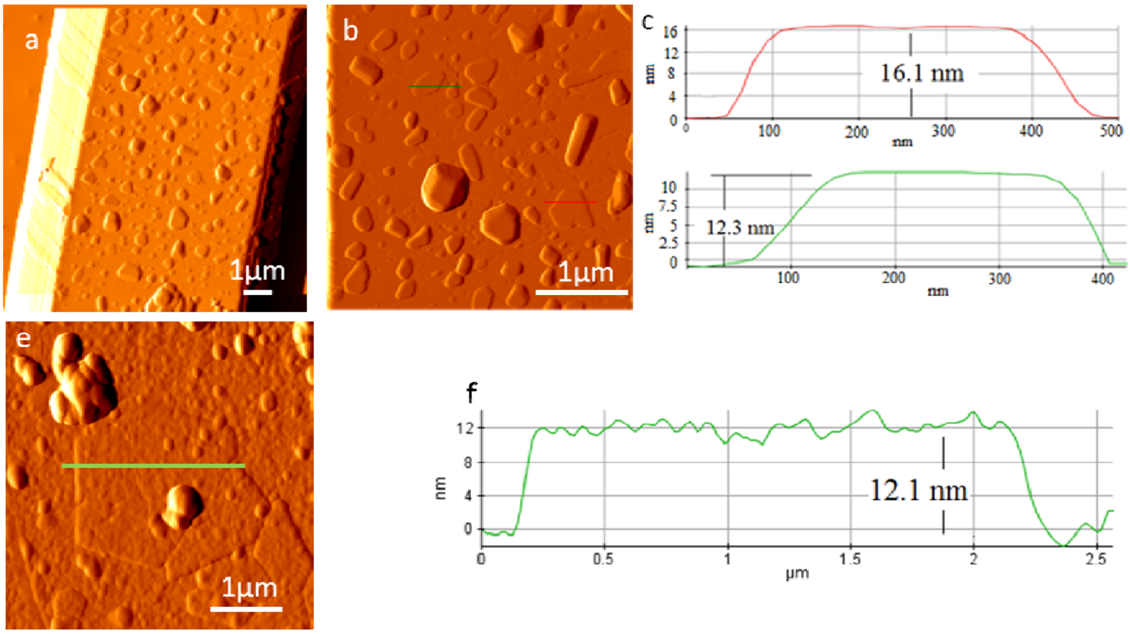

Figure 3. 16 AFM images and line profiles of ZSM-11 (110) face. (a) AFM overview image of ZSM-11 (110) face; (b) zoomed in image on crystal of (a); (c-d) cross-sectional profile of colored lines in (b); (e) AFM image of a thin lay structure; (f) line profile of green line on (e).

The growing features on different crystal faces are usually varied due to the different crystal planes they present [27,40,41]. Some work shows that each crystal face may have their own growing unit as well as growth morphology. To comprehensively investigate surface properties of ZSM-11, we also examined the (111) face of the zeolite with AFM and the results are presented in Figure 3. 17a. An overview image with the tip part of the crystal is shown in the Figure 3. 17. Due to the tilted angle between the tip and the AFM scanning plane, the 4-fold is not shown perfectly with right angles in the center. But we still can see four (111) faces embraced together. There are many large sized nuclei on all of the four faces but we can still find a small flat area for taking amplified image. Figure 3. 17b shows the amplified area in red square in Figure 3. 17a. The (111) face is also grown by a mechanism of merging nuclei i.e. birth and spread. The nuclei do not present round shape comparing to the (110) face due to different formation preference on (111). The cross-sectional profile is taken on a nucleus observed as newly born; the height profile shows its height is 11 nm. However, due to the extremely complicate repeating structure of (111) face, the height cannot be easily correlated to the framework structure.

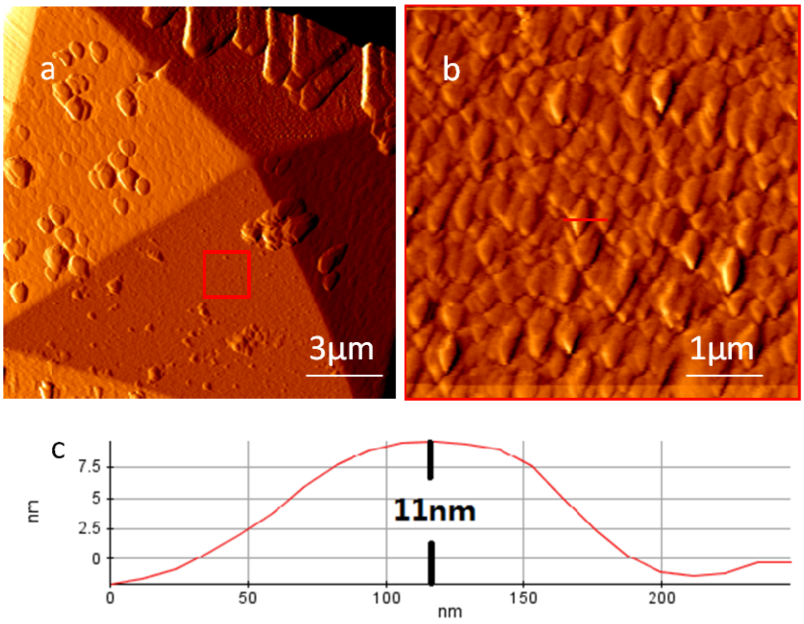

Figure 3. 17 (a) overview AFM image of crystal (111) face on ZSM-11; (b) amplified AFM image of (111) face; (c) cross-sectional profile of red line in (b).

3.4 Conclusion

In conclusion, ZSM-11 single crystal was successfully prepared under HTS condition with the presence of NH_4F and DPHMII. The crystallization was monitored by examining the samples with different reaction times. A comprehensive investigation was carried out by using XRD, NMR, SEM, and AFM. Crystalline structure of ZSM-11 was formed from the amorphous particles lacking long rang ordering, according to both of the XRD and NMR results. SEM images verified the morphologies at each reaction stage are consistent with structure evolution the XRD and NMR. Particularly, a careful AFM examination on crystal surface was carried out. Synthesized crystal showed typical tetragonal shape and perfect crystal surface for AFM study. Accurate measurement on surface nuclei specified the growing unit structure in ZSM-11 is the unit cell chains on (110) face. Re-grown crystal in diluted mother liquor presented abundant growing features. And the (111) crystal face was also presented by AFM. This chapter provides a clear picture of crystallization process of ZSM-11 by combination of the AFM, XRD, NMR and SEM results.

3.5 References

(1) Dorset, D. L. *Z. Kristall.* **2003**, *218*, 458.

(2) Liu, X. Y.; Su, W. H.; Wang, Y. F.; Zhao, X. D. *J. Chem. Soc.-Chem. Commun.* **1992**, 902.

(3) Argauer, R. J. L., G.R. *US patent 3702886* **1972**.

(4) Kokotailo, G. T.; Chu, P.; Lawton, S. L.; Meier, W. M. *Nature* **1978**, *275*, 119.

(5) Piccione, P. M.; Davis, M. E. *Microporous Mesoporous Mater.* **2001**, *49*, 163.

(6) Millward, G. R., Ramdas, S., Thomas, J. M., Barlow, M. T., *J. Chem. Soc. Far. Trans. 2* **1983**, *79*.

(7) Nakagawa, Y. *US. Patent 95 09812* **1995**.

(8) Bhange, D. S.; Ramaswamy, V. *J. Porous Mat.* **2012**, *19*, 301.

(9) Coudurier, G.; Auroux, A.; Vedrine, J. C.; Farlee, R. D.; Abrams, L.; Shannon, R. D. *J. Catal.* **1987**, *108*, 1.

(10) Harrison, I. D.; Leach, H. F.; Whan, D. A. *Zeolites* **1987**, *7*, 21.

(11) Kokotailo, G. T.; Lawton, S. L.; Olson, D. H.; Meier, W. M. *Nature* **1978**, *272*, 437.

(12) Yamamoto, S.; Sugiyama, S.; Matsuoka, O.; Kohmura, K.; Honda, T.; Banno, Y.; Nozoye, H. *J. Phys. Chem.* **1996**, *100*, 18474.

(13) Itzel Meza, L.; Anderson, M. W.; Slater, B.; Agger, J. R. *Phys. Chem. Chem. Phys.* **2008**, *10*, 5066.

(14) Moh, P. Y.; Cubillas, P.; Anderson, M. W.; Attfield, M. P. *J. Am. Chem. Soc.* **2011**, *133*, 13304.

(15) Li, S.; Falconer, J. L.; Noble, R. D. *Microporous Mesoporous Mater.* **2008**, *110*, 310.

(16) Zhang, L.; Bates, J.; Chen, D.; Nie, H.-Y.; Huang, Y. *The Journal of Physical Chemistry C* **2011**.

(17) Terasaki, O.; Ohsuna, T.; Sakuma, H.; Watanabe, D.; Nakagawa, Y.; Medrud, R. C. *Chem. Mater.* **1996**, *8*, 463.

(18) Agger, J. R.; Hanif, N.; Cundy, C. S.; Wade, A. P.; Dennison, S.; Rawlinson, P. A.; Anderson, M. W. *J. Am. Chem. Soc.* **2002**, *125*, 830.

(19) Gonzalez, G.; Stracke, W.; Lopez, Z.; Keller, U.; Ricker, A.; Reichelt, R. *Microsc. Microanal.* **2004**, *10*, 224.

(20) Fyfe, C. A., Lin, Z. S. *Efficient, Low-temperature Syntheses of Phase-pure Zeolite ZSM-11 (MEL framework)*, in preparation.

(21) Antoine Fecant, B. N. B., Feysin *US patent 05 0274875* **2008**.

(22) Chen, B. H.; Kirby, C. W.; Huang, Y. N. *J. Phys. Chem. C* **2009**, *113*, 15868.

(23) Ye, L. P.; Cao, F. H.; Ying, W. Y.; Fang, D. Y.; Sun, Q. W. *J. Porous Mat.* **2011**, *18*, 225.

(24) Davis, M. E. *Nature* **2002**, *417*, 813.

(25) Fyfe, C. A.; Brouwer, D. H.; Lewis, A. R.; Chézeau, J.-M. *J. Am. Chem. Soc.* **2001**, *123*, 6882.

(26) Fyfe, C. A.; Lin, Z. S.; Tong, C.; Darton, R. J. *Microporous Mesoporous Mater.* **2012**, *150*, 7.

(27) Cubillas, P.; Stevens, S. M.; Blake, N.; Umemura, A.; Chong, C. B.; Terasaki, O.; Anderson, M. W. *J. Phys. Chem. C* **2011**, *115*, 12567.

(28) Wakihara, T.; Sasaki, Y.; Kato, H.; Ikuhara, Y.; Okubo, T. *Phys. Chem. Chem. Phys.* **2005**, *7*, 3416.

(29) Sunagawa, I. *Crystals: Growth, Morphology and Perfection*; Cambridge University Press, **2005**.

(30) Pablo Cubillas, M. W. A. *Zeolites and Catalysis: Synthesis, Reactions and Applications* **2010**, Wiley.

(31) Binnig, G.; Quate, C. F.; Gerber, C. *Phys. Rev. Lett.* **1986**, *56*, 930.

(32) Garcia, R.; Perez, R. *Surf. Sci. Rep.* **2002**, *47*, 197.

(33) Wakihara, T.; Sugiyama, A.; Okubo, T. *Microporous Mesoporous Mater.* **2004**, *70*, 7.

(34) Dumrul, S.; Bazzana, S.; Warzywoda, J.; Biederman, R. R.; Sacco, A. *Microporous Mesoporous Mater.* **2002**, *54*, 79.

(35) Holme, B.; Cubillas, P.; Cavka, J. H.; Slater, B.; Anderson, M. W.; Akporiaye, D. *Crystal Growth & Design* **2010**, *10*, 2824.

(36) Meza, L. I.; Anderson, M. W.; Agger, J. R. *Chem. Commun.* **2007**, 2473.

(37) Wakihara, T.; Okubo, T. *J. Chem. Eng. Jpn.* **2004**, *37*, 669.

(38) Ohsuna, T.; Slater, B.; Gao, F. F.; Yu, J. H.; Sakamoto, Y.; Zhu, G. S.; Terasaki, O.; Vaughan, D. E. W.; Qiu, S. L.; Catlow, C. R. A. *Chem. Eur. J.* **2004**, *10*, 5031.

(39) Morales, J.; Astilleros, J. M.; Fernández-Díaz, L. *Cryst. Growth Des.* **2011**, *12*, 414.

(40) Cubillas, P.; Holden, M. A.; Anderson, M. W. *Cryst. Growth Des.* **2011**, *11*, 3163.

(41) Anderson, M. W.; Agger, J. R.; Hanif, N.; Terasaki, O.; Ohsuna, T. *Solid State Sci.* **2001**, *3*, 809.

Chapter 4 Surface Investigations of Microporous Materials

4.1 Introduction

By using a number of characterization techniques on the problem of the microporous materials growth, it is possible to discover detailed nucleation and crystal growth mechanisms [1,2]. In particular, AFM has emerged as a powerful technique to study the crystallization of microporous materials due to its nanometer scale resolution of surface features. By scanning the surface with nanometer scale probe, the effects of supersaturation and temperature on crystal growth become more apparent at this fundamental scale. Understanding the growing parameters provide possibilities to better control the crystal size, morphology and surface properties.

Due to their molecule-sized channels and cages, zeolites are often referred as molecular sieves. Another important type of molecular sieves is aluminophosphate ($AlPO_4$)-based materials, which were discovered by the workers at Union Carbide Corp. in 1982 [3]. The frameworks of AlPO4s are similar to those of the zeolites. However, instead of built up by Si-O-Si or Si-O-Al linkages in the zeolites, $AlPO_4$s are composed of Al-O-P linkages [4]. Since the frameworks of $AlPO_4$s are charge neutral, consequently, there is no Brønsted acidity. That limits their application as catalysts. Nevertheless, the incorporation of Si into the structure of $AlPO_4$s generates negatively charged framework, and thus provides possibility of using the corresponding materials, silicoaluminophosphates (SAPOs), as acid catalysts. The common linkages in SAPOs are Si-O-Al, Si-O-Si and P-O-Al, while Si-O-P linkages are proved to be energetically unstable.

Among SAPO-based molecular sieves, SAPO-34 is of particular importance due to its potentials for several applications including gas separation and water adsorption [5]. Moreover, it is considered as one of the most effective catalysts in the conversion of methanol to olefins (MTO) [6]. According to the reported SAPO-34 studies, it can be prepared using a number of structure-directing agents (SDA), as well as be synthesized by different methods like HTS and DGC [6]. Its framework is analogous to that of the natural zeolite chabazite, where the framework type code CHA derived from. The 2-dimenstional building units of the framework are 4- or 6-membered rings in which Si, Al, P tetrahedral sites locate on vertices with O atoms linking in between. Two 6-member rings are linked with six 4-member rings to form double 6-rings (Fig 4. 1a) as the secondary building units. These double 6-rings (D6Rs) joined together by four-membered rings to build up the framework structure (Figure 4. 1b) containing the eight-ring system with a diameter of 0.38 nm (Fig. 4. 1c). Till now, a number of studies on the synthesis of SAPO-34 have been reported under HTS condition, including an AFM study recently [7].

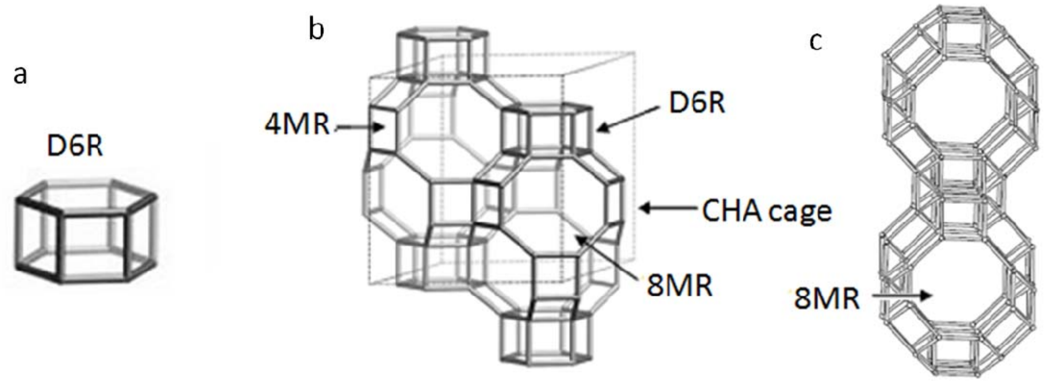

Figure 4. 1 Illustration of framework structure of SAPO-34 (a) double 6-ring; (b) framework structure of SAPO-34; (c) structure view along 8-ring channels.

Another important SAPO-base material, SAPO-37, has attracted attention from the point of view of its catalytic performances [8,9]. SAPO-37 is usually prepared by hydrothermal synthesis method (HTS) from an aqueous hydrogel prepared by mixing phosphoric acid, alumina oxide and fumed silica as well as structure-directing agents (SDAs). Its framework belongs to Faujasite (FAU) structure type, which is similar to those widely used zeolites in industrial such as Zeolite X, Zeolite Y and zeolite Faujasite. Several AFM studies also have been carried out on these zeolites [1,10,11], but no studies reported on the surface properties of this SAPO-based material. The framework type of

SAPO-34 is FAU, which has the secondary building units D6R and Sodalite (SOD) cage. In the framework structure, each SOD cages share the 6-rings with D6Rs to form a large cavity with 12-ring window. The cavity is called FAU cage (Figure 4. 2).

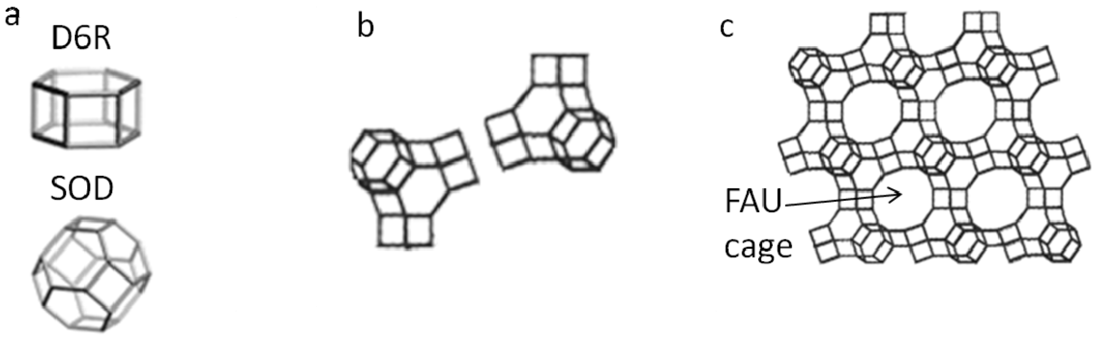

4. 2 Illustrations of framework structure of SAPO-37 (a) D6R and SOD cage; (b) connection type of D6R and SOD cage;(c) framework structure of SAPO-37.

Another high silica zeolite, ZSM-39 (framework structure MTN), has been studied in terms of its unique structure with 17 Å cubic gas hydrate [12]. ZSM-39 is usually synthesized hydrothermally. The large crystals can be synthesized [13]. Therefore, it is a promising candidate for AFM study. The structure of ZSM-39 is composed of two types of cages, those with twelve 5-rings ($[5^{12}]$ cage) and cages with twelve 5-rings and four 6-rings ($[5^{12}6^4]$ cage, Figure Figure 4. 3). The framework structure is built by sharing the face of these two kinds of cages.

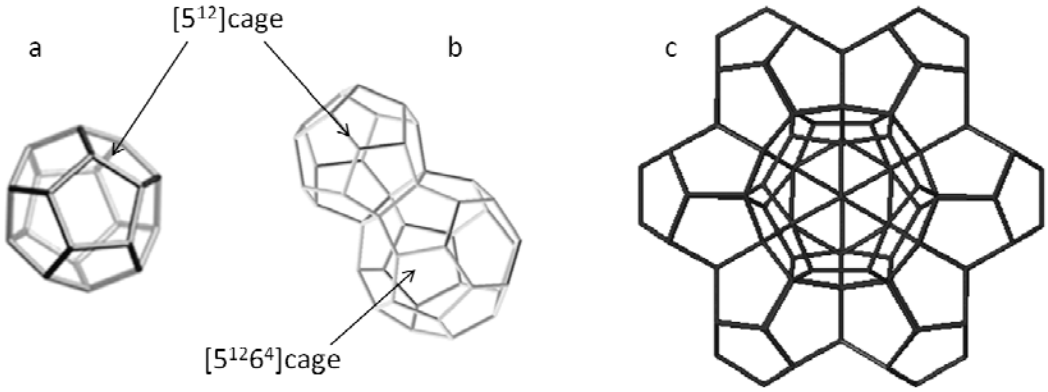

Figure 4. 3 Illustration of framework structure of ZSM-39. (a) MTN cage; (b) connection type of MTN cage and [$5^{12}6^4$] cage; (c) framework structure of ZSM-39.

In this chapter, surface structures of three zeolitic materials are investigated. For SAPO-34, both HTS and DGC synthesized samples are both examined carefully by AFM. The observations provide information on the growth behaviors under different synthetic conditions. From this information, possible growth mechanisms can be derived. In the study of SAPO-37, AFM characterization is presented for the first time. Attention was paid not only to the surface morphology but also terminated structures. For ZSM-39, AFM images of two different faces shows significant difference of surface structure. The difference is interpreted in terms of the growth preference of crystal faces and morphology.

4.2 Experimental Details

4.2.1 Sample preparation

The SAPO-34 crystals were prepared by two different synthesis methods, HTS and the DGC, as described in Chapter 2. In this section, experimental details are presented.

The HTS synthesis of SAPO-34 was conducted according to the method reported in literature [14,15]. The reagents used were pseudo-boehmite (Catapal-B, ca. 65wt% Al_2O_3), H_3PO_4, morpholine ($O(CH_2CH_2)_2NH$), colloidal silica (LUDOX Am-30, Sigma-Aldrich) and distilled water. The mole ratio of the original gel was 2.1morpholine: 1.0SiO_2: 1.0Al_2O_3: 1.0P_2O_5: 60H_2O. A typical procedure of the gel preparation is following: in beaker A, 15.6g of Catapal B, 23.0 g H_3PO_4, and 44.0 g H_2O were mixed and stirred vigorously for 10 min before adding additional 22.0 g H_2O. In beaker B, 20.0 g silica gel, 18.4 g mopholine and 20.0 g H_2O were combined; this solution was then slowly added to the mixture in beaker A during intense stirring. At the end of the gel preparation, 4.0 g HF was added into the gel. This reaction mixture was then separated into several Tefon-lined autoclaves and heated in an oven at 200 ˚C. After specific reaction time, the autoclaves were quenched into cold water to stop the reaction. The solid phase was separated from the liquid phase by centrifugation, dried in air at room temperature, and kept in sealed glass vials for analysis.

The DGC synthesis of SAPO-34 was carried out by the method reported previously [16,17]. The reagent used were pseudo-boehmite (Catapal-B, Vista, ca. 65% Al2O3), H_3PO_4 (EM Science, 85%), diethylamine (Alfa Aesar), colloidal silica (Ludox LS-30, Aldrich) and distilled water. The initial dry gel molar ratio is $1.0Al_2O_3$:$0.8P_2O_5$:$0.4SiO_2$:2.0DEA: $50H_2O$. A typical procedure for the preparation of dry gel is the following: 15.7 g of Catapal B was mixed with 76.1 g of distilled water, and the mixture was stirred at room temperature for 10 minutes before adding 18.4 g of H_3PO_4 slowly with continuous stirring. The solution containing 8 g of colloidal silica and 14.6 g of DEA which was also stirred for 10 minutes at room temperature was then slowly added to the above mixture under vigorous stirring for homogeneity. The final mixture was stirred for 1 h and then dried at 80 ˚C with constant stirring to allow evaporation of water until white solids formed. The solid sample was then ground into a fine powder and sealed in glass vials. A series of intermediates were synthesized by placing 1.0 g of the initial dry gel powder into small Teflon cups. Each cup was placed in a 23-mL Teflon-lined autoclave with 0.4 g distilled water at the bottom and heated in an oven at 200˚C for different times. The reactions were quenched in cold water after specific reaction time. Obtained solid was dried and sealed in glass vial for further analysis.

Samples of SAPO-37 and ZSM-39 are provided by my colleagues Lu and Sonia, respectively.

SAPO-37 was prepared under HTS condition with heating the mixture of silion and aluminum source with the SDA, tetramethylammonium hydroxide pentahydrate (TMAOH·$5H_2O$). The reaction temperature is 170 ˚C for 2 days.

ZSM-39 sample was synthesized in tetramethylammonium chloride/1, 6-hexanediol deep eutectic solvent using NH4F as the mineralizing agent. And kept at 140˚C for 14 days.

4.2.2 Characterization

Powder XRD patterns of intermediate samples were recorded on a Rigaku diffractometer with Co Kα radiation (λ=1.7902 Å). SEM analysis was performed on a LEO 1540XB field emission scanning electron microscope.

AFM used in surface structure study is a Park Systems XE-100. A cantilever with nominal spring constant of 40 N/m, resonant frequency of 300 kHz and tip radius of 10 nm (NSC15, Mikro Masch) was operated under the dynamic force mode. In this mode, the cantilever is vibrated at around the resonant frequency and its amplitude reduces when the tip is in proximity with the sample surface caused by the tip - sample interaction. Reduced amplitude is set as the feedback parameter (set point) so that the AFM system scans the surface contour of the sample with minimized error signals (the difference between the set point and the amplitude measured) by adjusting the distance between the tip and the sample surface. Mapping of this distance constructs topographic image for the surface morphology. Mapping the error signal results in an image removing the height contribution and stressing only the shape of surface features. When the height range is large, surface features with small height differences are obscured. In this case, it is advantageous to use the error signal image to show the shapes of surface features, while using the topographic image to estimate the height distribution. The scan rate for obtaining images in an area of 45×45 μm^2 is 0.5 Hz and for images in an area of 10×10 μm^2 is 1 Hz. The experiment was conducted in air with a relative humidity of ~40%.

4.3 Results and Discussion

4.3.1 SAPO-34

In this section, we examined surface properties of SAPO-34 prepared by two different methods, HTS and DGC. The main objectives are to gain information regarding the nucleation, crystal growth behavior, and the effects of synthesis condition on the crystal growth, thus illustrate the possible connections between of HTS and DGC synthesis methods. Very recently, growth mechanisms of SAPO-34 under hydrothermal synthesis conditions with morpholine as SDA were examined [18] and the results provided benchmark for interpretation of our data. In order to illustrate the possible synthesis mechanism differences between these methods, we re-examine SAPO-34 prepared by HTS first and use the results to illustrate the features of SAPO-34 samples prepared by dry gel conversion.

SAPO-34 prepared by HTS

SAPO-34 single crystals were prepared by the HTS method described in the experimental details. Figures 4. 4a and b show the microscopic images of SAPO-34 single crystals. The crystals are very large (up to 50 µm). All the upward faces in the images are rhomboidal, whose two internal angles are around 100˚ and 80˚ respectively. As the framework structure of SAPO-34 belongs to the trigonal crystal system, both hexagonal and rhombohedral unit cell are possible. Since no 120˚ angle on the rhomboidal face was observed, we assign the crystal unit cell to rhombohedral system. A three-by-three rhombohedral unit cells arrangement illustrated in Figure 4. 4c is well consistent with the crystal morphology in microscopic images. The crystal faces shown in microphraphs could be assigned to (001) face in rhombohedral system. Therefore, the *a* axis is along the direction labeled as [100]; the *b* axis is along the direction labeled as [010]; and the *c* axis is pointing out of the paper plane perpendicularly. The crystals of the SAPO-34 synthesized by the HTS have large surface, which make it easy for further AFM probe locating. There is no obvious debris and nuclei particles on the surface, thus detailed surface features in micro scale could be captured accurately.

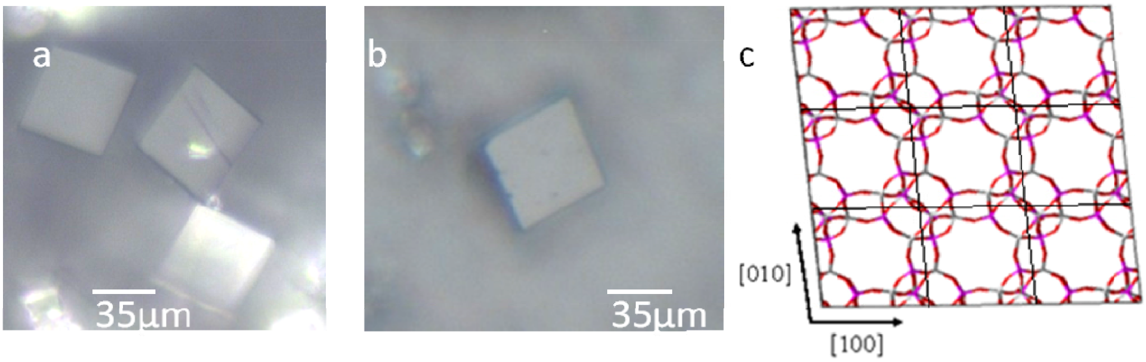

Figure 4. 4 (a) and (b) microscopic images of SAPO-34 single crystals synthesized by the HTS; (c) scheme of 3×3 rhombohedral unit cells arrangement.

Figure 4. 5a is an overview image of AFM error signal on a crystal of SAPO-34. Because the topographic image has a large height range, which obscures the visualization of the crystals having small height differences, error signal image is shown here. The upward face of the crystal is a rhombus with 100° and 80° degree angles and the edge length are around 50 µm, which is consistent with the observation of microscopy. Partial intergrowth can be found at the lower left part and the central part of the image. Except these two spots, the (001) face is clean and flat. Zooming in the flat area at the right side area of the central intergrowth structure, a number of particles were found on the crystal surface (Figure 4. 5b). The particles are sized from 40 to 150nm in diameter, and some of which merge into a larger cluster as showed in the center of the image. The particles are the crystal nuclei formed at the end of crystallization. And the aggregation behavior is indicative of "adhesive" growth mechanism, regarding the relatively high level local supersaturation. The large particle structures on crystal surface indicate the high supersaturation on this particular area.

Figure 4. 5c shows an amplified image of flat area on crystal surface in Figure 4. 5b and step structures are presented clearly in this image. Instead of showing regular geometric shape, the steps prefer to located one on the top of another all over the (001) face. Instead of showing regular straight edge, the steps have edges with serrate line. Pseudo-pentagonal shaped hillock spiral was not observed in our study as in Holme's work [18]. The height information of the labeled red line is shown in the cross-sectional profile at the lower part of Figure 4. 5c (cross-section height profiles were taken from the topographic image). The curve shows homogeneous steps height of 0. 9±0.1nm. The spacing between steps represents a flat terrace with around 50 nm in width. The step growth of surface indicates a "birth and spread" growth mechanism, which usually occur when the solution is at a relatively low supersaturation. Figure 4. 5d is the only spiral feature that observed on the hydrothermal sample of the SAPO-34 crystals. Even no perfect hillock spiral structure with regular geometry was found, an obvious line defect

could be observed at this “U” shaped spiral. This observation amplifies the mechanism of spiral growth in crystallization. Based on the surface features in Figures 4. 5b, c and d, surface nuclei and steps are discovered on the same crystal face, which specifies that the two growth mechanism occurred on the same crystal simultaneously. This phenomenon indicates that the growth environment on the surface is not homogeneous. Supersaturation varies at different area on the same crystal face.

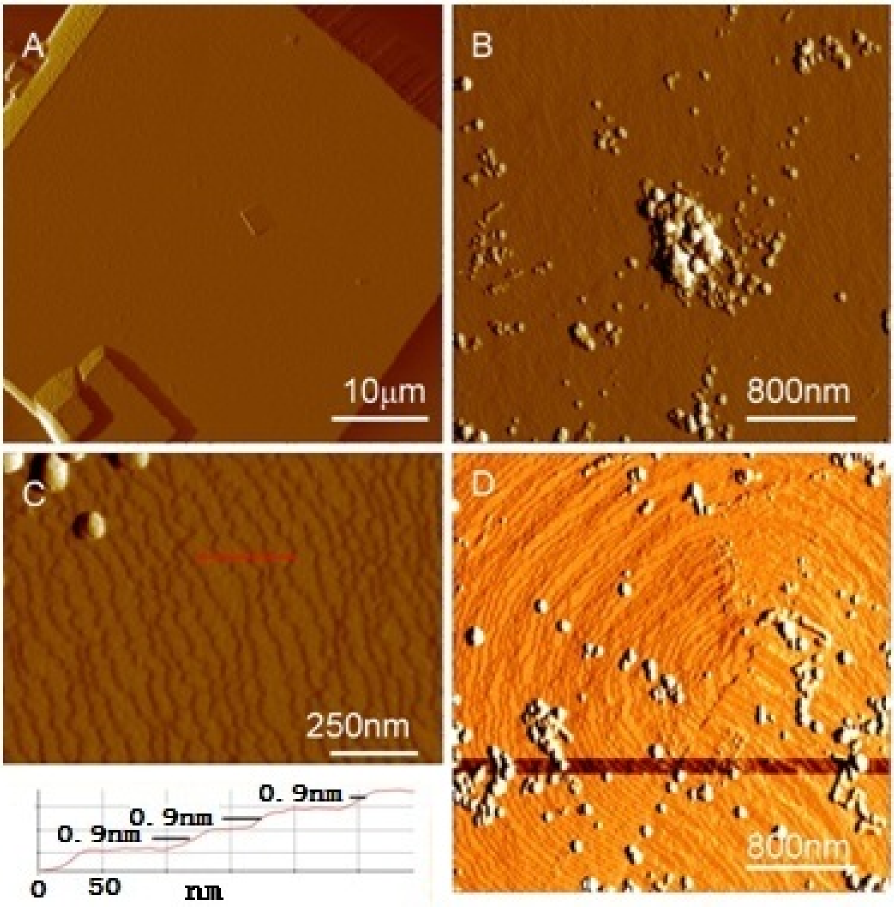

Figure 4. 5 AFM Images of SAPO-34 (a) top view of one crystal; (b) zoomed-in image of particle clusters on (a); (c) zoom in image on flat area of (b); (d) spiral-like structure on sample surface.

The observed step with height of 0.9±0.1 nm on the (001) face can be correlated to the framework structure. In the structure type of the SAPO-34, every D6R connects to the other four D6Rs in (001) plane (Figure 4. 6a) and linking to the D6Rs in the layers above and underneath. Thus, tilted D6Rs connections form D6R-sheet structures in (001). There is a side view scheme shown in Figure 4. 6b, which shows three D6R layers connecting along [001] direction. Theoretical distance between two sheets is 0.94 nm[19]. The steps height measurement from the AFM image, which is 0.9±0.1 nm, is well consistent to the distance between tilted D6R layers. This indicates that the crystals have single sheets of the D6R on the external surface. Both the theoretical structure parameter and the experimental data indicate that the 0.9 nm step is the minimum growth structure (D6R sheets) in SAPO-34 crystals. Such conclusion is consistent with that reported by Holme et, al[18].

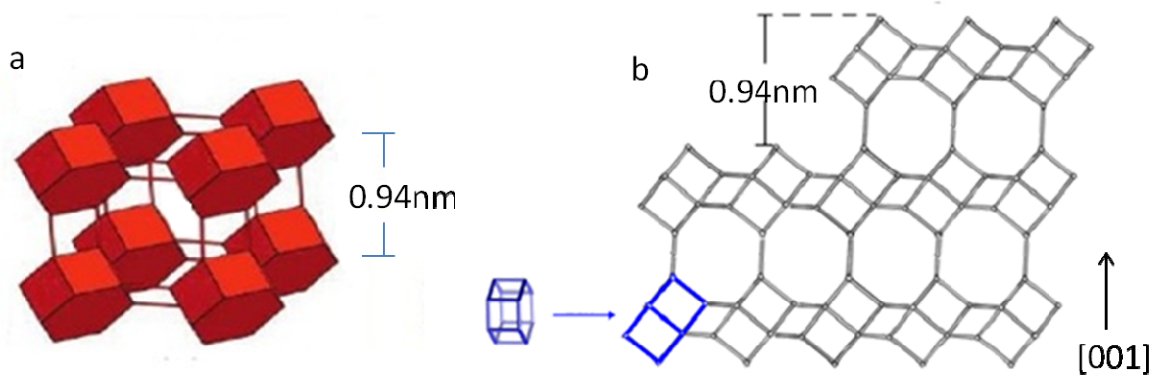

Figure 4. 6 SAPO-34 Framework structure (a) Simplified drawing D6Rs connection structure; (b) (111) projection of D6Rs layered structure.

SAPO-34 prepared by DGC

The SAPO-34 single crystals were also obtained by the DGC method described in the experimental details. The crystallization was monitored by powder-XRD on both series of washed samples and unwashed samples (XRD patterns is shown in Appendix 1, experiments were carried out by Ms. Lu Zhang). The patterns of unwashed initial gel has sharp reflections with strong low angle peak, which means that the major component of the initial dry del is layered material with long-rang ordering. Upon heating, the peaks due to the layer structure gradually become weaker and broader. The crystal layered phase becomes a semi-crystalline material. Further heating the sample for 2 days resulted in the emergence of several sharp peaks whose positions correspond to (101), (211), and (300) reflections of SAPO-34. However, the pattern also contains the peaks due to AlPO4-11, known as a competing phase[20]. The 5-day sample only contains peaks due to SAPO-34, and no peak of AlPO4-11 is seen in the pattern. This process indicates that the SAPO-34 formed from layered structures that are held by weak, noncovalent bonding interactions. Upon washing, all the reflection due to the semi-crysatlline layered phase disappeared in corresponding XRD patterns.

Figure Figure 4. 7a shows the SEM image of SAPO-34 prepared by DGC approach. Based on the crystal morphology and the AFM work on SAPO-34 prepared by HTS, the crystal surface can be assigned to the (001) face of rhombohedral unit cell. For the SAPO-34 samples prepared by DGC methods, the crystal surfaces are often covered by a significant amount of surface debris even after extensive washing. Therefore, finding the crystals with good surface conditions suitable for AFM analysis is very challenging and time consuming. Nonetheless, few crystals with relatively good surface conditions were found and present good conditions for AFM scanning. The AFM images of one of such crystals are shown in Figure Figure 4. 7b. Due to the maximum scanning area of the AFM instrument used (45×45 μm^2) is smaller than the crystal face (60×60 μm^2), four AFM images of (001) face containing four corners from the same crystal were recorded separately and piecing them together to provide the outline of the 2D surface (Figure Figure 4. 7b). "Pseudo-rectangular" terraces parallel to [100] and [010] directions can be found at several locations on the same crystal surface (two such terraces are shown inside the blue box inside Figure Figure 4. 7b). The spiral growth was previously observed on the (001) face of the SAPO-34 crystals synthesized with morpholine as SDA under HTS conditions [18], but no such spiral was found for the SAPO-34 crystals prepared by the DGC method . The magnified image (Figure Figure 4. 7c) shows the rough surface and multiple nucleation points on the surface, suggesting that the crystal growth mechanism is "birth and spread"[21]. Under VPT conditions employed in this study, the nucleation rate appears to be fast as evident from many nuclei on the crystal surface. These nuclei quickly spread and coalesce to form surface terraces.

Analysis of cross-section profiles for four individual freshly formed nuclei sitting on relatively flat terraces (the ones inside red circles in Figure Figure 4. 7c) shows that the average height of the nuclei is 22.5 nm (Figures Figure 4. 7d-e show the cross-sectional depth profile of two such nuclei). There are several nuclei (see the ones inside blue circles in Figure Figure 4. 7c) whose heights are about 10 nm. However, these nuclei have already partially merged with the terraces underneath.

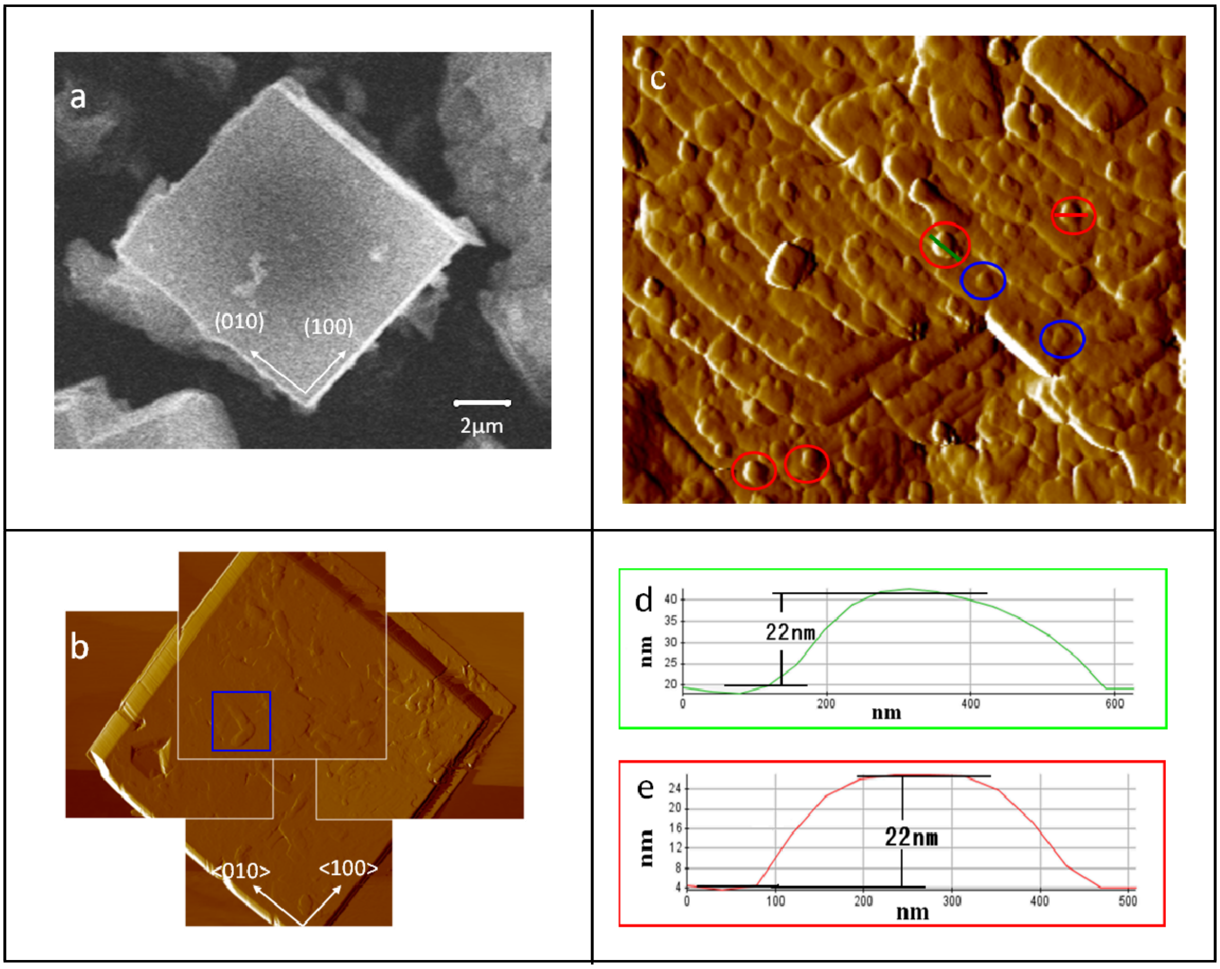

Figure 4. 7 SEM and AFM images of the [001] face of SAPO-34 crystals (DGC 7 d sample): (a) SEM image of a crystal (b) top-view AFM images (error signals are shown here for clarity) of another large crystal, each image taken in size of 45 ×45

μm^2; (c) enlarged view a square area in (b), 10 ×10 μm^2; (d) and (e) cross-section height profile from the topographic image (not shown) along different lines in as shown in (c), showing the height of two nuclei.

The average nuclei height is 22.5 nm, which is much larger than that (0.9 nm) found for the crystals synthesized by HTS method [18]. SAPO-34 structure is built upon the D6Rs joint together via single 4-memebered rings. The height of the terrace (0.9 nm) reported corresponds to the repeat distance (0.94 nm) between the layers of the tilted D6Rs along [100] direction. In the present work, the average height of nuclei formed under DGC conditions is 22.5 nm, corresponding to about 23 layers of D6Rs.

The AFM results provide some details that can be included in SAPO-34 formation mechanism under DGC conditions proposed earlier. Unlike hydrothermal synthesis where nutrients can come from liquid phase, all the reactive species in DGC are contained in the solid phases. The small amount of bulk water is separated from the dry gel, which eliminates the direct contact between the reactive species in solution and solid gel. The small amount of water in vapor is not enough to dissolve the solids. Therefore, the formation of SAPO-34 is unlikely through gel dissolution and therefore the single D6R layer growth was not observed. The conversion from the precursor to SAPO-34 is likely the water assisted solid to solid transformation. The forces holding the sheets together are weak non-bonding interactions. The weak interactions facilitate bond breaking and re-forming in the absence of bulk liquid and therefore assist in the transformation from the layered phase to SAPO-34. Such transformation likely occur in a small domain involving several sheets of D6Rs in the precursor at once via cooperative reorganization of local structure of P and Al as well as Si species in the vicinity. The number of the sheet in the precursor involved in each domain may be estimated from XRD and AFM data. From the XRD pattern of 3 h sample the interlayer spacing can be estimated at 1.3 nm. Thus, observed nuclei with a height of 22.5 nm, corresponding to 23 layers of D6Rs in SAPO-34, may result from the simultaneous transformation of 23 sheets of precursor (with a total height of 30 nm). Such nucleation process is illustrated in

Figure 4. 8. Seeing many nuclei in Figure Figure 4. 7c indicates that the transformation happens in many locations within the precursor.

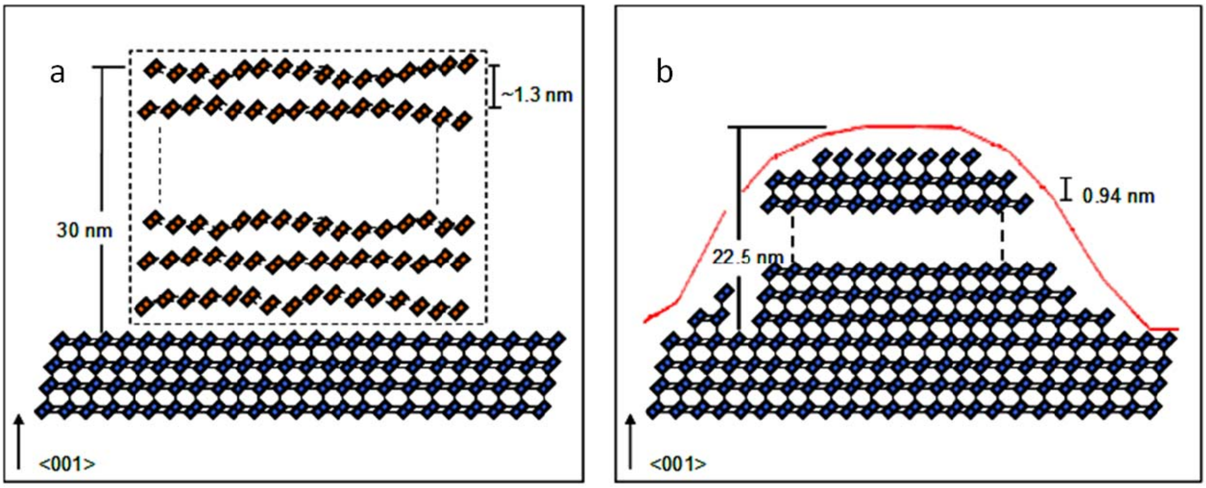

Figure 4. 8 Illustration of nucleus formation on (001) face. (a) 23 sheets of precursor with a total height of about 30 nm; (b) A SAPO-34 nucleus containing 23 D6R with a height of 22.5 nm.

4.3.2 SAPO-37 by HTS

Several studies on the crystal growth of the FAU structure such as zeolite Y and zincophosphate-faujasite (ZnPO-FAU) have been reported [22-25]. In the present study we utilize AFM to scan the surface of SAPO-37 crystals synthesized by HTS method. To date, this is the first study to observe nucleation and growth of SAPO-37 crystals by AFM.

Figures 4.9 show SEM images of SAPO-37 crystals. The Figure 4.9a shows the overview image of several crystal grains and most of the crystals exhibit regular octahedral shape. According to the crystal morphology, the triangular face on octahedral crystal can be assigned to (111) face. Figure 4.9b shows an amplified image on (111) face of SAPO-37. It shows the crystal have flat surface with triangular shape, which is suitable for AFM to work on the surface.

Figure 4. 10a shows the AFM image of the SAPO-37 crystals in the 4d samples. The AFM image only presents one triangular-shaped (111) face on each of the octahedral crystal grains. Figure 4. 10b depicts an 8×8 μm^2 AFM image of one of the (111) faces. Besides the intergrown structure at the face centre, several triangular steps can be found on the surface, which are more apparent in Figure 6c. The magnified image (Figure 4. 10c) presents a rough (111) surface covered with multiple steps and nuclei, suggesting that the crystal growth mechanism is “birth and spread” [21]. Similar surface structures were reported before on the (111) face of the ZnPO-FAU crystals [26]. Section analysis (Figures 4. 10d and e) reveals that the terraces and nuclei in Figure 4. 10c have an average thickness of approximately 7.5 and 10.5 nm, which corresponds to the thickness of about 5 and 7 FAU layers with each layer of 1.43 nm thick, respectively [24]. A thickness of one unit layer of FAU structure was previously observed on the (111) surface of the zeolite Y and ZnPO-X (analogous to zeolite X) crystals synthesized under HTS conditions [22,24,25]. Under this synthesis conditions, both the heights of terraces and nuclei have much larger sized than the reported value in zeolite mateirals [11,27].

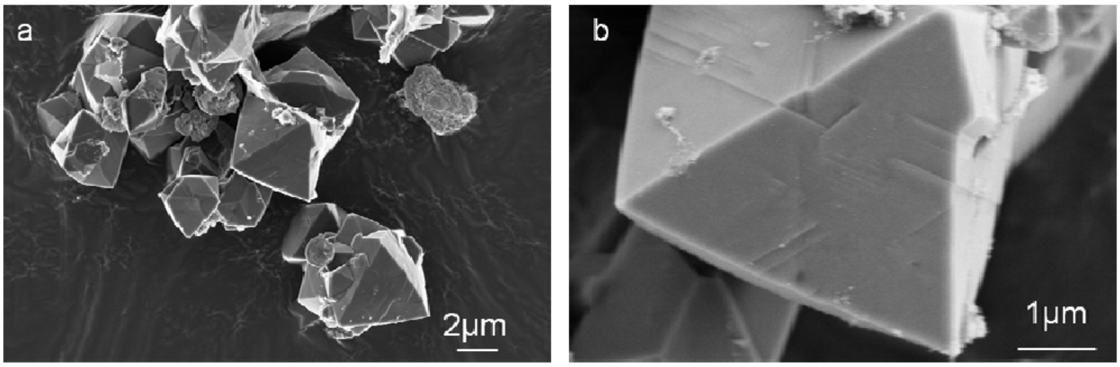

Figure 4.9 SEM images of SAPO-37 (a) overview image on a group of crystals with octahedral morphology; (b) amplified image on one (111) face of crystal.

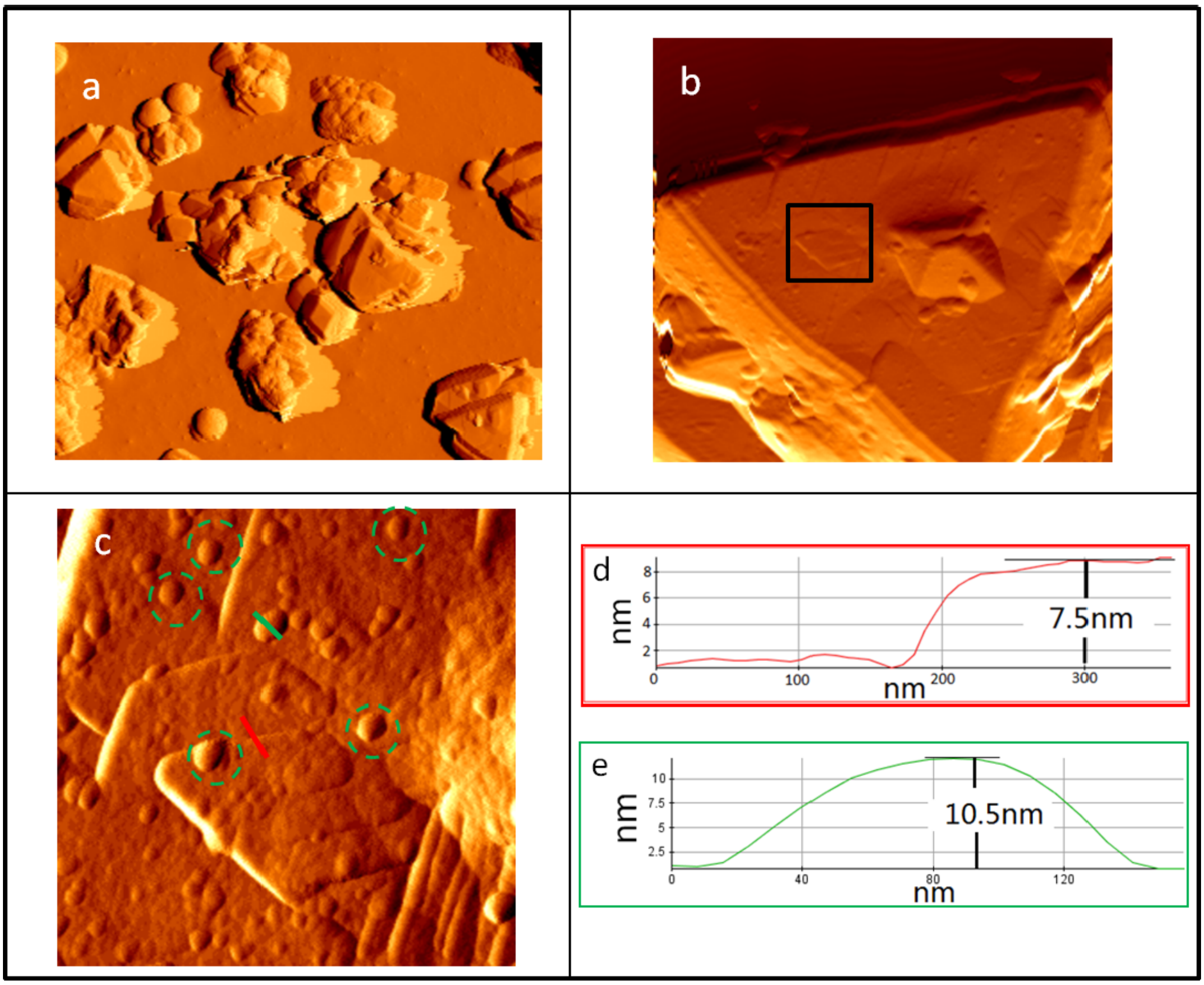

Figure 4. 10 AFM images of the (111) faces of SAPO-37 crystals (4 d sample). (a) top-view image in the size of 45×45 µm^2; (b) image in size of 8×8 µm^2; (c) enlarged view of a square area in the black box in (b) image in sized of 2×2 µm^2 ; (d) and (e)

cross-sectional height profile from the topographic image along red and green lines shown in (c), showing the average height of surface steps and nuclei.

Besides the above surface structures on the SAPO-37 crystals, other growth features were also observed. Figure 4. 11a shows one (111) face of another crystal. A magnified image of it (Figure 4. 11b) indicates that the steps on its surface have triangular shapes rotated by 60° relative to the crystal edges, which is consistent with the findings reported by Anderson and co-workers in the study of zeolite Y [24]. Figure 4. 11c shows a (111) face of a crystal with a large hollow at the center of the surface. This indicates that SAPO-37 crystals have preference for growing on the edges first and then towards the center, which is similar to the growth pattern of ZnPO-FAU in solution [25]. Further, some triangle-shaped dent pits were observed on the surface edge of the same crystal face. The appearance of these dent pits suggest that several layers of triangular steps may form first on the same surface. They then grew and coalesced together. An illustration of how the dent pits are formed from triangular steps is shown in Figure 4. 11d. The merging of the two triangular shaped layer indicates the spread behavior in the “birth and spread” growth mechanism.

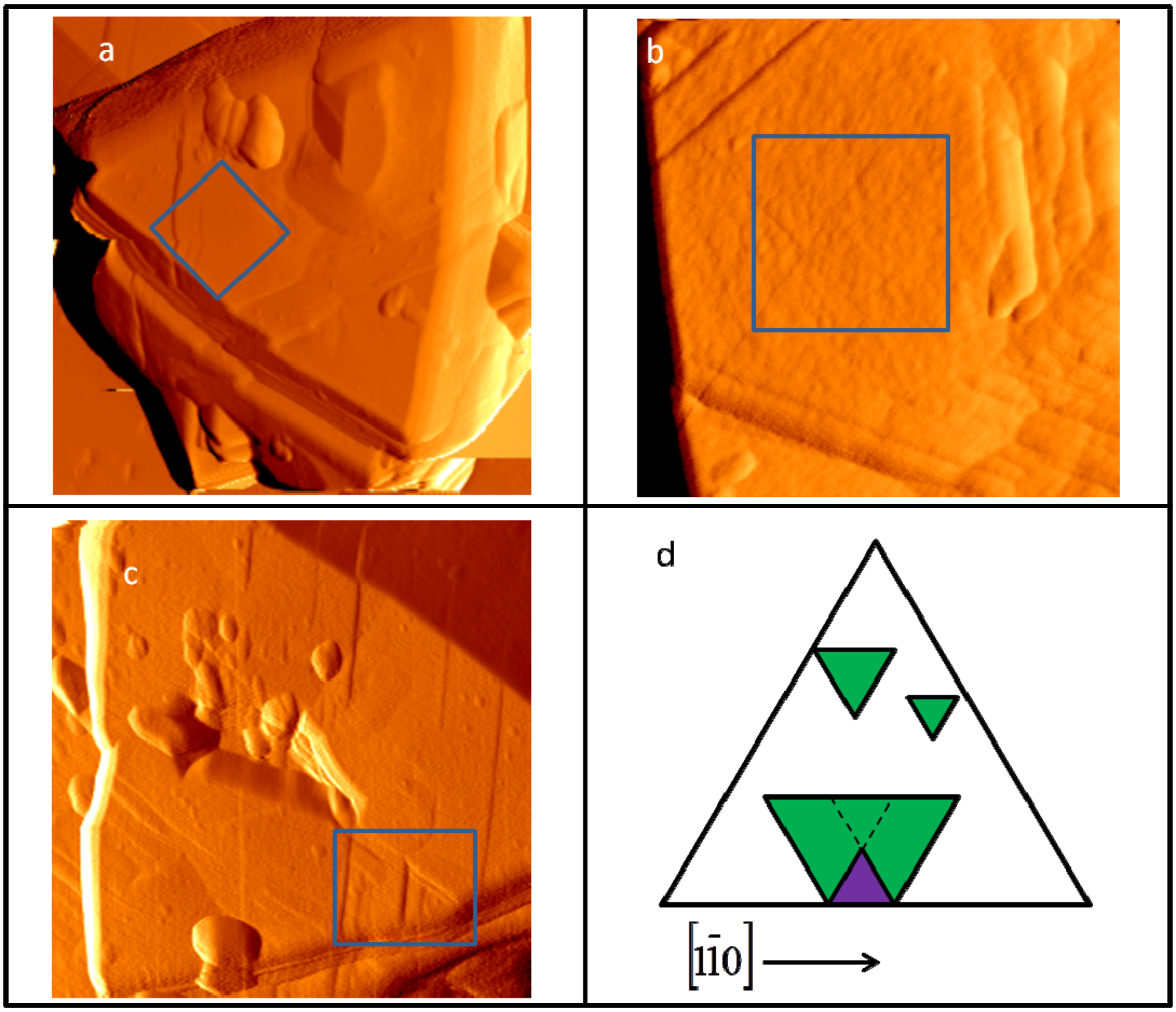

Figure 4. 11 (a) AFM image of a (111) face on a crystal in the size of 8×8 µm^2; (b) zoomed-in image of the blue square area in (a); (c) AFM error signal image of a (111) face on a crystal in the size of 4×4 µm^2; (d) an illustrative scheme of triangle-shaped steps and dent pits on the (111) surface.

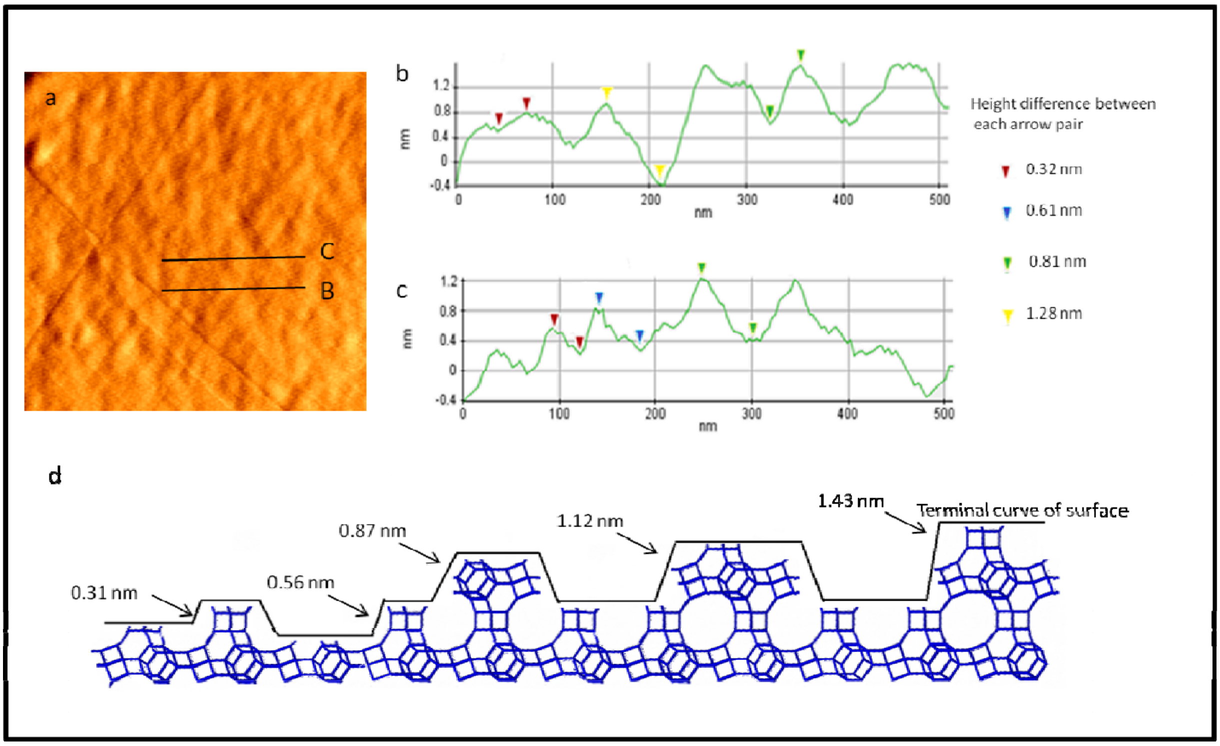

Figure 4. 12 (a) AFM image of the boxed area in Figure 4. 11b on a crystal in the size of 800×800 nm^2; (b-c) cross- sectional profiles along the lines in (a). Heights of ca. 1.28, 0.87, 0.56 and 0.31 nm are observed; (d) a model of the terminal structure of SAPO-37 along the lines in (a).

The central part of Figure 4. 11b shows a relatively flat area. However, after zooming in (Figure 4. 12a), it is interesting to notice that the surface is not as flat as it appears and heights smaller than integral magnitudes of 1.43 nm are observed. Two cross-sectional lines are drawn on the flat part and their heights profiles are shown in Figures 4. 12b and c. The height information in the two cross-sectional lines shows peaks with various heights such as 0.31 nm (6-membered ring, 6R), 0.56 nm (double 6-membered ring, D6R), 0.87 nm (incomplete sodalite cage) and 1.28 nm (between 1.12-nm-high complete sodalite cage and 1.43-nm-high one FAU layer). The height changes in the line are obviously beyond the scanning error of the probe (<0.1 nm). So they can be assigned to framework structure. Multiple steps with heights less than 1.43 nm were previously observed on the (111) face of the zeolite Y crystals grown in the aluminosilicate solutions [22]. By modeling the observed terminal structures, it was reported that complete D6Rs were the major surface structure. However, no such steps but rough surfaces with different microstructures are observed for the SAPO-37 crystals prepared by the HTS method. These results demonstrate that instead of having uniform terminal structures on the surface, the (111) face of SAPO-37 crystals prefers to be terminated by different microstructures such as 6Rs, D6Rs and incomplete sodalite cages (Figure 4. 12d), under the experimental condition employed.

4.3.3 ZSM-39 by DES

We take ZSM-39 as another example to study some of the high silicate zeolite. The crystals in the SEM (Figure Figure 4. 13) image have relatively large sizes (grain size goes up to 70 μm). All crystals show a pseudo-cubic shape with six square faces and eight pseudo-triangle faces. Two crystals with these typical faces upward are amplified and shown in the image. Both of these face types are large sized flat faces where AFM could easily scan on. Also, crystal surfaces have rarely large debris or over sized nuclei, which provide good conditions for AFM scanning.

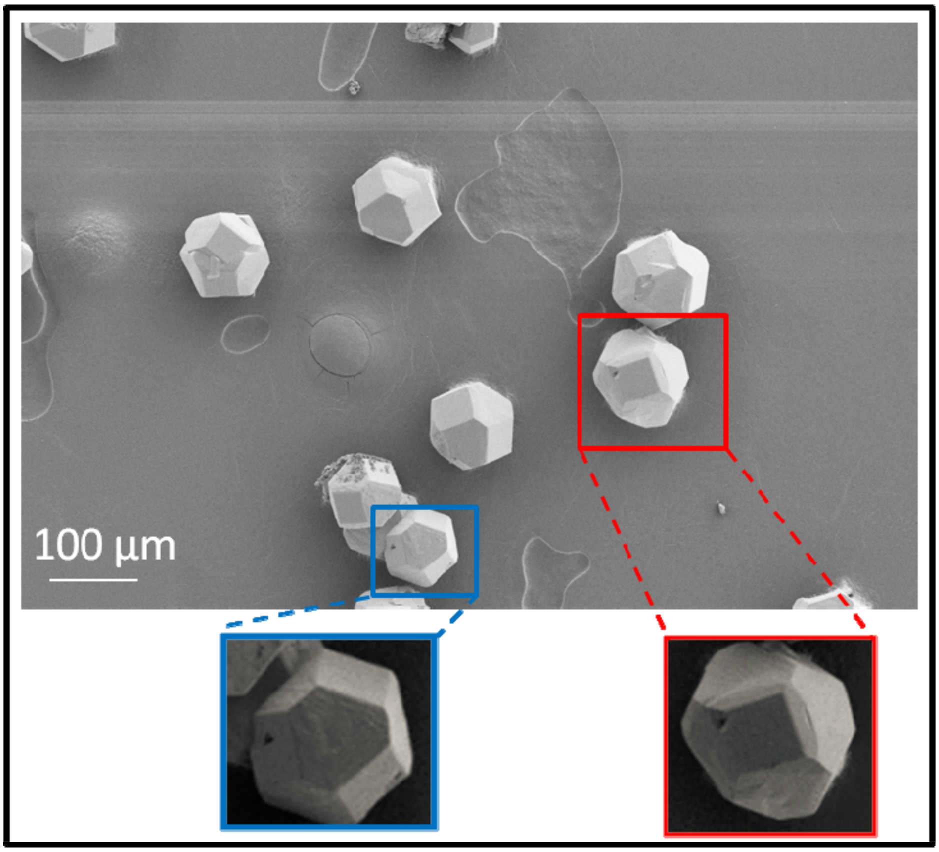

Figure 4. 13 SEM image of ZSM-39 crystals and two typical face amplified image.

Morphology evolution mechanism of crystals in cubic system was investigated in Anderson's work on FAU structure [11]. The scheme shown in Figure 4. 14 represent how eight triangular faces enlarge and merged into six-face-truncated octahedron. With the growth of the black truncated triangular faces, the crystal grain grows larger as well as terminates the six square faces and finally develops into a regular octahedron with only eight triangular (111) faces. Crystal morphologies in ZSM-39 samples synthesized by eutectic solvent have the similar morphology as the middle of the revolution (Figure 4. 14c). But as shown by the AFM results demonstrate that the case in ZSM-39 differ from FAU in that the growing faces are not the triangular (111) faces but the (100) square face.

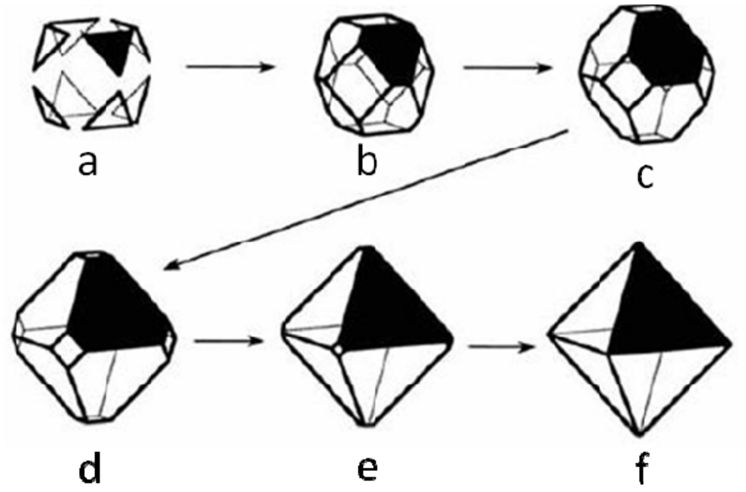

Figure 4. 14 Illustration of the morphology evolution of crystal in cubic system [11].

The AFM results of ZSM-39 are shown in Figure 4. 15 and all the AFM image in this figure are shown in the largest scanning sized AFM could provide (45×45 μm^2). In Figure 4. 15a, an overview image of ZSM-39 (001) face is shown and the surface is a very flat face with a square shape. The surface contains nuclei but there is an area that present flat crystal face. In Figure 4. 15b, a corner of the square face shows that the angle is perfect 90 degree and the edge are very clear. There are minor crystal faces observed along the edges. Figure 4. 15c shows the (100) face on the crystal morphology.

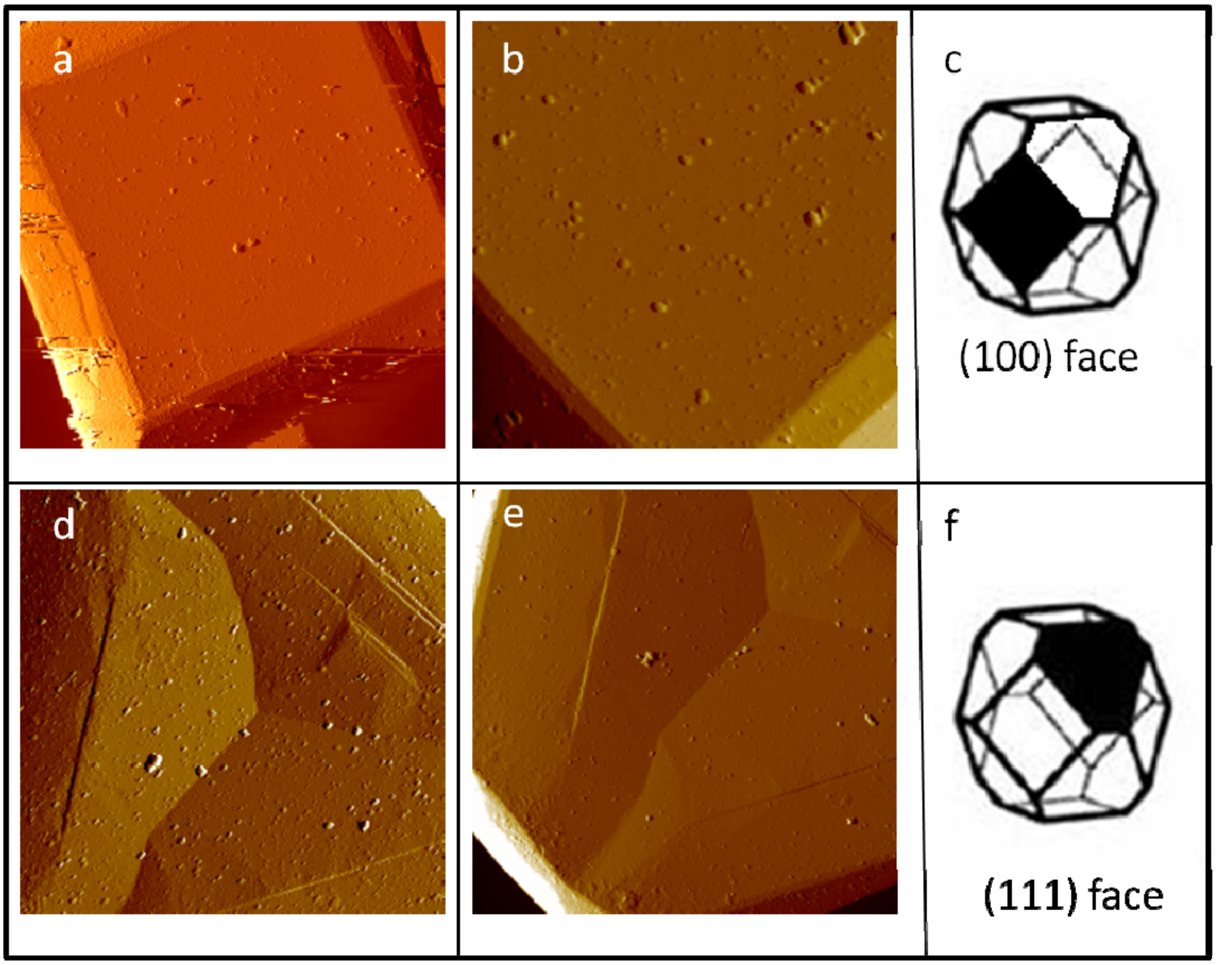

Figure 4. 15 AFM image of ZSM-39 (a-b) overview AFM image on (100)faces. (b) overview faces on (111) faces.

Figure 4. 15d and e show crystal (111) faces on two different crystals. Figure 4. 15f shows their position on the crystal morphology. Interestingly, the pseudo-triangular (111) face of crystal is not a flat face with layered structure as observed in Anderson's study on zeolite Y [11]. The faces are not flat and show obvious 3-fold symmetry grooves. In the center of the face, a lowest point is shown and there are three piece of crystal faces piecing together to form this pseudo-triangle shape. The grooves run along the bisector

for each truncated angles. And the edge of the pseudo triangle is merging with the squares' edge. The 3-fold symmetry grooves indicate that the triangle face is not a face that was formed by self-motivated growing (which mostly presents a flat face). According to the Anderson's work, the triangle faces should be the one that motivated grown [11]. However, in our work, the squared face is the one grown faster.

As AFM is able to achieve accurate measurement of surface morphology, we detected the micro scale features. In our studies, surface nuclei on (100) face were measured. In Figure 4. 16 a, the overview AFM image shows that there are a number of large nuclei on the crystal surface and the sizes range from 150-800 nm in lateral and 30-150 nm in height. They are very large nuclei. To capture the detailed morphological features on smaller scale, amplified image on a very flat area in size of 1×1 μm^2 is shown in Figure 4. 16. Some nuclei in this area appear to be newly born isolated nuclei and others have merged together. The cross-sectional profile shown blow is one of the newly born nuclei with sharp outline. For two nuclei in the red circles, their dimensions are 2 nm in height and 50 nm in lateral. Therefore, the nuclei observed from the AFM image is more like a thin terrace. In Figure 4. 16, the framework structure shows that along the direction of the surface, the terrace structure could be correlated to one layer of the primary building units (MTN cages). Therefore, the nuclei in the figure above could be correlated to one layer of the building units.

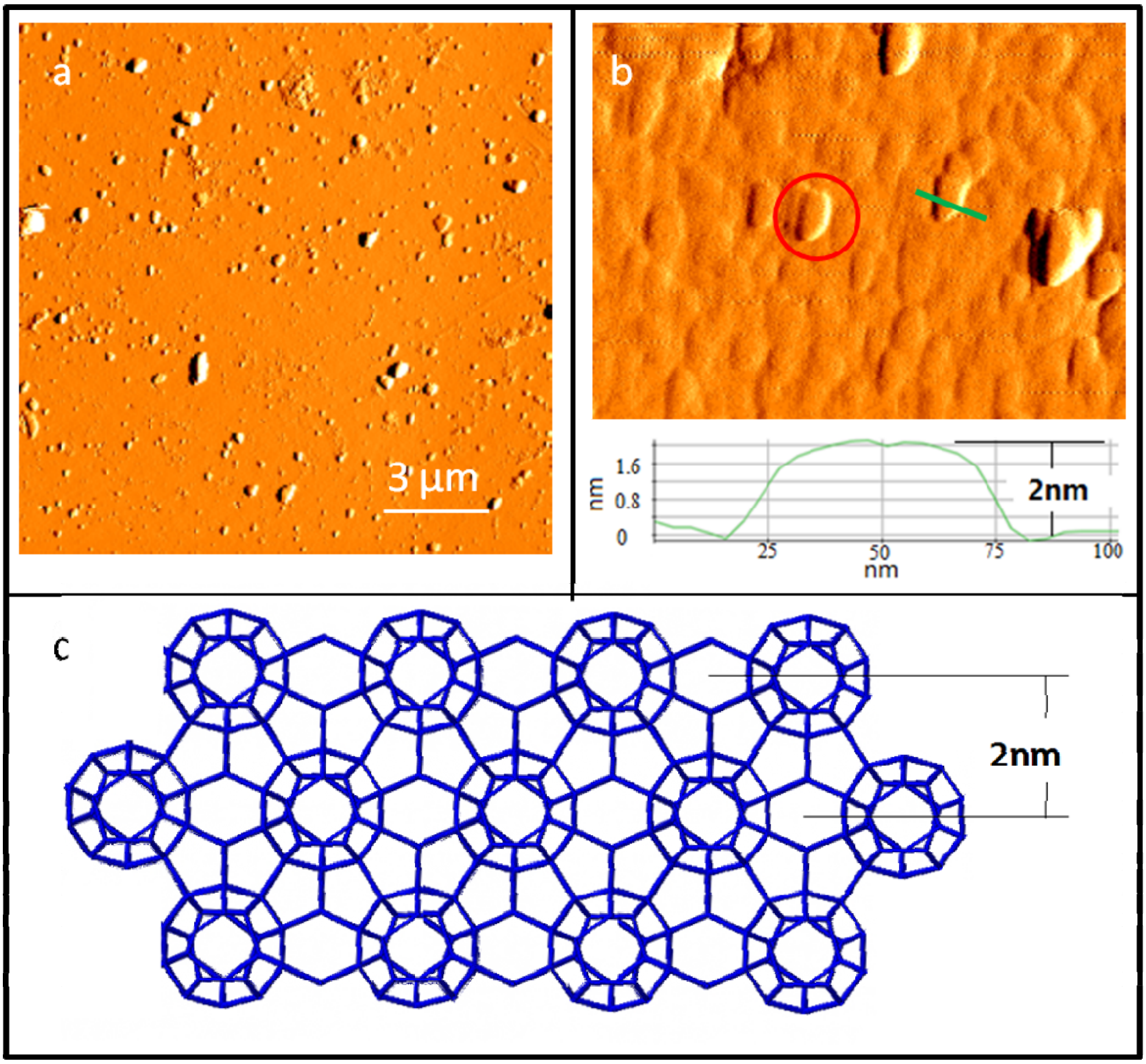

4. 16 (a) AFM image on (100) face of ZSM-39; (b) amplified image on flat area and cross-sectional profile; (c) illustration scheme of (100) face 2nm nuclei.

4.4 Conclusion

By using AFM, the surface features of the several microporous materials were investigated and correlated to their framework structures. For SAPO-34, crystals synthesized from different methods, HTS and DGC, show diverse surface morphologies. The surface features on (001) faces indicate that the crystal from HTS was growing layer by layer of the structure of double 6-rings, whereas the DGC crystal was forming large nuclei that contains 23 double 6-ring sheet structure. SAPO-37 presented growing features as another FAU framework material. Study on its surface termination was carried out and different terminal structures on surface were observed. For ZSM-39, the high silicate zeolite gain large crystal size in Ionothermal Syntheses. Both flat face of (100) and face with 3-fold symmetry grooves were observed, which indicated the different growth rate of these two different faces.

4.5 References

(1) Cubillas, P.; Holden, M. A.; Anderson, M. W. *Cryst. Growth Des.* **2011**, *11*, 3163.

(2) Cubillas, P.; Stevens, S. M.; Blake, N.; Umemura, A.; Chong, C. B.; Terasaki, O.; Anderson, M. W. *J. Phys. Chem. C* **2011**, *115*, 12567.

(3) Wilson, S. T.; Lok, B. M.; Messina, C. A.; Cannan, T. R.; Flanigen, E. M. *J. Am. Chem. Soc.* **1982**, *104*, 1146.

(4) Sastre, G.; Lewis, D. W.; Richard, C.; Catlow, A. *J. Phys. Chem. B* **1997**, *101*, 5249.

(5) Li, S. G.; Falconer, J. L.; Noble, R. D. *J. Membr. Sci.* **2004**, *241*, 121.

(6) Schnabel, K.-H.; Fricke, R.; Girnus, I.; Jahn, E.; Loffler, E.; Parlitz, B.; Peuker, C. *J. Chem. Soc., Faraday Trans.* **1991**, *87*, 3569.

(7) Holme, B.; Cubillas, P.; Cavka, J. H.; Slater, B.; Anderson, M. W.; Akporiaye, D. *Cryst. Growth Des.* **2010**, *10*, 2824.

(8) Fernandes, G. J. T.; Fernandes Jr, V. J.; Araujo, A. S. *Catal. Today* **2002**, *75*, 233.

(9) Zamadics, M.; Kevan, L. *J. Phys. Chem.* **1993**, *97*, 10102.

(10) Moh, P. Y.; Cubillas, P.; Anderson, M. W.; Attfield, M. P. *J. Am. Chem. Soc.* **2011**, *133*, 13304.

(11) Anderson, M. W.; Agger, J. R.; Thornton, J. T.; Forsyth, N. *Angew. Chem. Int. Ed.* **1996**, *35*, 1210.

(12) Bibby, D. M.; Parker, L. M. *Zeolites* **1983**, *3*, 11.

(13) Schlenker, J. L.; Dwyer, F. G.; Jenkins, E. E.; Rohrbaugh, W. J.; Kokotailo, G. T.; Meier, W. M. *Nature* **1981**, *294*, 340.

(14) Yan, Z.; Chen, B.; Huang, Y. *Solid State Nucl. Magn. Reson.* **2009**, *35*, 49.

(15) Vistad, Ø. B.; Akporiaye, D. E.; Taulelle, F.; Lillerud, K. P. *Chem. Mater.* **2003**, *15*, 1650.

(16) Chen, B.; Huang, Y. *J. Am. Chem. Soc.* **2006**, *128*, 6437.

(17) Chen, B.; Huang, Y. *J. Phys. Chem. C* **2007**, *111*, 15236.

(18) Holme, B.; Cubillas, P.; Cavka, J. H.; Slater, B.; Anderson, M. W.; Akporiaye, D. *Cryst. Growth & Des.* **2010**

10, 2824.

(19) Yamamoto, S.; Sugiyama, S.; Matsuoka, O.; Kohmura, K.; Honda, T.; Banno, Y.; Nozoye, H. *J. Phys. Chem.* **1996**, *100*, 18474.

(20) Tapp, N. J.; Milestone, N. B.; Bibby, D. M. *Zeolites* **1988**, *8*, 183.

(21) Cubillas, P.; Anderson, M. W. **2010**.

(22) Wakihara, T.; Sugiyama, A.; Okubo, T. *Microporous and Mesoporous Materials* **2004**, *70*, 7.

(23) Wakihara, T.; Okubo, T. *Journal of chemical engineering of Japan* **2004**, *37*, 669.

(24) Anderson, M. W.; Agger, J. R.; Thornton, J. T.; Forsyth, N. *Angew. Chem. Int. Ed. in English* **1996**, *35*, 1210.

(25) Cubillas, P.; Holden, M. A.; Anderson, M. W. *Cryst. Growth Des.*

(26) Singh, R.; Doolittle Jr, J.; George, M. A.; Dutta, P. K. *Langmuir* **2002**, *18*, 8193.

(27) Wakihara, T.; Sugiyama, A.; Okubo, T. *Microporous Mesoporous Mater.* **2004**, *70*, 7.

Chapter 5 Summary and Suggestions on Future Work

5.1 Summary

In this thesis, crystal growth of several zeolites and microporous materials was investigated using AFM. In chapter 3, ZSM-11 single crystal was successfully prepared under HTS condition. Crystalline structure of ZSM-11 was formed from the amorphous particles lacking long rang ordering, according to both of the XRD and NMR results. SEM images verified the morphologies developed consistent with XRD and NMR results. Synthesized crystal showed typical tetragonal shape and perfect crystal surface for AFM study. Accurate measurement on surface nuclei specified the growing unit structure in ZSM-11 is the unit cell chains on (110) face. Re-grown crystal in diluted mother liquor presented layered structures which indicate the birth and spread growth mechanism. And (111) face was formed by surface nuclei. In chapters 4, SAPO-34 crystals synthesized from different methods, HTS and DGC, show diverse surface morphologies. The surface features on (001) faces indicate that the crystal from HTS was growing layer by layer of the structure of double 6-rings, whereas the DGC crystal was forming large nuclei that contains 23 layers of double 6-ring sheets. SAPO-37 presented growing features as another FAU framework material. Study on its surface termination was carried out and different terminal structures on surface were observed. For ZSM-39, the high silicate zeolite gain large crystal size in Ionothermal Syntheses. Both (100) flat face and (111) face with 3-fold symmetry grooves were observed, which indicated the different growth rate of these two different faces.

5.2 Suggestions on Future Work

By finishing this thesis, we have obtained some knowledge in crystal surface features and their relationship with the framework structure. We also gained experience in AFM operation on powder samples. However, there are many problems remained for further investigation.

Regarding the synthesis methods, a stable, long reaction time normally gives single crystals with large surfaces that provide AFM ideal working environments for AFM study. Most zeolite crystals could be prepared under HTS. So this synthesis method is still recommended to obtain single crystals with large size. For AFM technique, in-situ observation is worthy trying for monitor change on surface in real time. However, ex-situ method is also an efficient way to study the crystal growth.

Appendices

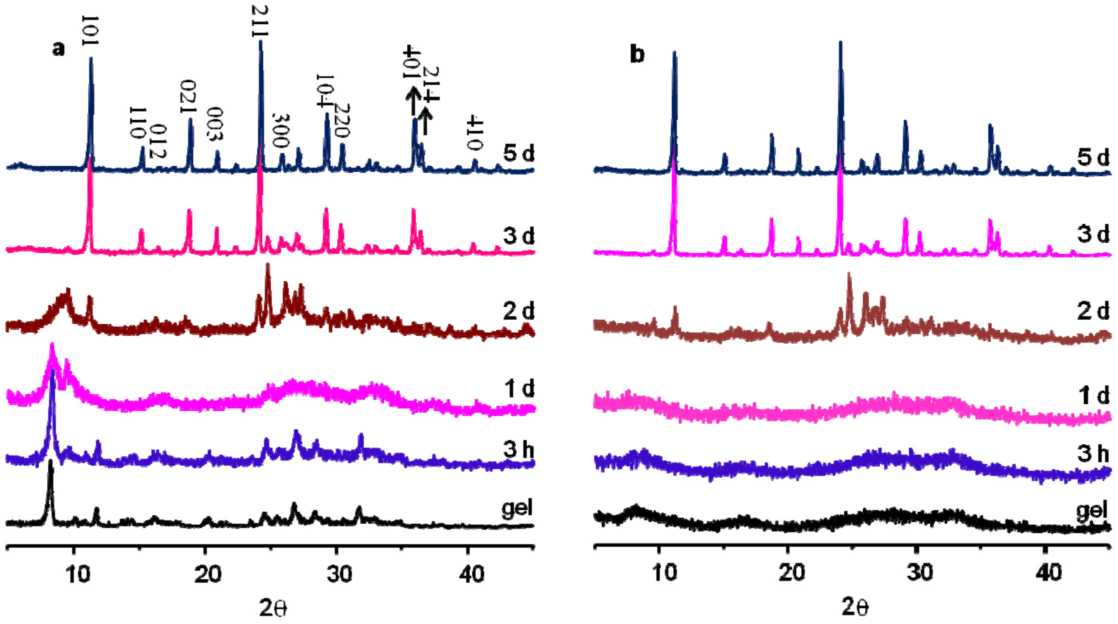

Appendix 1: Powder XRD patterns of SAPO-34 samples prepared by DGC (A) unwashed SAPO-34 samples and (B) washed samples.

Title: Investigations of Formation of Molecular Sieve SAPO-34

Author: Lu Zhang, Jennifer Bates, Donghan Chen, Heng-Yong Nie, and Yining Huang

Publication: The Journal of Physical Chemistry C

Publisher: American Chemical Society

Date: Nov 1, 2011

Copyright © 2011, American Chemical Society

If you're a copyright.com user, you can login to RightsLink using your copyright.com credentials. Already **a RightsLink user** or want to learn more?

Welcome to Rightslink

American Chemical Society has partnered with Copyright Clearance Center's Rightslink service to offer a variety of options for reusing American Chemical Society content. Select the "I would like to ..." drop-down menu to view the many reuse options available to you.

Appendix 2: Copyright Release from Publisher for part of the Chapter 4.

Curriculum Vitae

Name:	Donghan Chen
Post-secondary Education and Degrees:	University Science and Techonology of China Hefei, Anhui, China 2006-2010 B.Sc. The University of Western Ontario London, Ontario, Canada 2010-2012 M.A.
Related Work Experience	Teaching Assistant The University of Western Ontario 2010-2012

Publication:

1. Zhang, L., Bates, J., Chen. D., Nie, H.-Y., Huang, Y., (2011) Investigations of Formation of Molecular Sieve SAPO-34, Journal of Physical Chemistry C, 115, 22309-22319.

Presentations:

1. Chen, D., Nie, H.-Y., Huang, Y., (2011) Investigation of Zeolite Growth by Atomic Force Microscopy, Poster presentation, CAMBR Distinguished Lecture and Research Day, University of Western Ontario, London, Ontario
2. Chen, D., Nie, H.-Y., Huang, Y., (2011) Investigation of Zeolite Growth by Atomic Force Microscopy, Oral presentation, Inorganic Discussion Weekend, Niagara Falls, Ontario
3. Chen, D., Zhang, L., Lin, Z.S., Nie, H.-Y., Huang, Y., (2012)) Investigation of Zeolite Growth by Atomic Force Microscopy, Poster presentation, International Scanning Probe Microscopy Conference, Toronto, Onrario